Neoproterozoic marine chemostratigraphy, or eustatic sea level change?

Gregory J. Retallack [*], Adrian P. Broz, Larry S.-H. Lai, Kevin Gardner

Department of Earth Sciences, University of Oregon, Eugene, Oregon 97403-1272, , USA

ABSTRACT

Paleosols are characterized with new chemical and petrographic data from the Tonian (776–729 Ma) Chuar Group in the eastern Grand Canyon, Arizona. Paleosols have been discovered at 66 stratigraphic levels in a 1622 m sequence largely of marine shales and thin intertidal stromatolitic dolostones. A purple paleosol association includes gypsum "desert roses" in profiles like Gypsids of hyperarid climates. A red paleosol association includes calcareous nodules profiles like Calcids of semiarid climates. Degree of weathering and phosphorus depletion of the paleosols is evidence of microbial-earth communities gaining in productivity during the Tonian. The gypsic to calcic soil transition in the modern Atacama Desert of Chile corresponds with a transition from simple actinobacterial-cyanobacterial microbial earths to complex algal-fungal communities of markedly greater weathering effectiveness and carbon sequestration. A similar change in biological weathering may have induced Snowball Earth 12 Myrs after deposition of the Chuar Group. Paleosols are found only at levels of the Chuar Group where $\delta^{13}C$ isotopic composition of both organic matter and of carbonate are below marine and mantle values. Although such inflections in isotopic time series have been considered chemostratigraphic markers of global oceanic composition, in this case we interpret them to reflect a change in sea level from shallow marine to terrestrial. A notable inflection at about 752 Ma in the Chuar Group corresponds with the recently recognized Konnarock Glaciation of Virginia, and may have been a time of global sea-level fall. Correlation of Precambrian marine sequences by wiggle matching isotopic time series may still be effective, but because of sea-level change rather than for the chemical oceanographic reasons originally envisaged.

1. Introduction

A widely used approach to correlating Precambrian rocks is wiggle-matching, now improved by fitting algorithms (Hay et al. 2019), of isotopic or other chemical time series, on the assumption that they represent changes in global ocean chemistry (Dehler et al. 2005; Swanson-Hysell et al. 2012). The trouble with this chemostratigraphic approach is that some observed fluctuations are unbelievable, unless the Proterozoic ocean was markedly different from Phanerozoic oceans in recording unique extreme events (Hoffman and Schrag 2002). For example, the mid-Ediacaran Shuram-Wonoka isotopic anomaly is both huge ($\Delta^{13}C$-carbonate of 12‰ and $\Delta^{13}C$-organic of 8‰) and prolonged (580 m corresponding to 17 Myr for carbonate, but <1 Myr for organic $\Delta^{13}C$), so is it a marine signal in submarine canyons (Giddings et al. 2010; Grotzinger et al. 2011), or were the paleovalleys excavated by rivers and the prolonged anomaly created by meteoric weathering and dissolution of canyon walls (Husson et al. 2012; Retallack et al. 2014)? Another example is the Ediacaran degree of sediment oxidation ranging

from anoxic (highly reactive to total iron, or Fe_{HR}/Fe_T ratios >0.38) to as oxidized as modern well drained soils (Fe_{HR}/Fe_T ratios <0.2) over just a few meters in supposed deep-sea sediments (Canfield et al. 2007), or were they actually shallow-marine sediments alternating with paleosols (Retallack 2013, 2016a)? Another example is an order of magnitude earliest Ediacaran acidification (0.7–1.7 pH unit decline) in the world ocean inferred from $\delta^{11}B$ ratios within <50 m of Ediacaran cap carbonates (Ohnemueller et al. 2014), which would be an incredible perturbation for such a large body of water, but not for paleosols in calcareous loess (Retallack 2011a). It is time to reexamine the default assumption that most analyzed Precambrian rocks are marine, and look more carefully at early diagenetic anomalies, including soil formation (Dehler et al. 2005; Swanson-Hysell et al. 2012). What would be geochemical extremes for oceans are unremarkable within paleosols (Retallack 2011a, 2013; Retallack et al. 2014), and instead may represent sea-level regression and subaerial weathering of sediments.

The purpose of this study is to examine the possibility that sea-level change caused a transition from marine rocks to subaerial weathering

and the formation of soils as an explanation for extreme isotopic perturbations (Δ^{13}C-organic of 20‰, and Δ^{13}C-carbonate of 16‰) and iron speciation values (Fe_{HR}/Fe_T 0.1 to 1.1) in the Tonian (776–729 Ma) Chuar Group in the eastern Grand Canyon, Arizona (Dehler et al. 2005, 2017; Johnston et al. 2010). Paleosols have not been previously recognized in the Chuar Group, because it has been difficult to recognize paleosols before the Silurian advent of rooted plants (Retallack 2015a, 2015b), and described Ediacaran paleosols (Retallack 2016b) have been challenged because they host trace and body fossils long assumed to have been marine (Gehling and Droser 2013).

A secondary aim of this work is to reassess evidence from the Chuar Group for paleoenvironments immediately prior to the Cryogenian (717–635 Ma) glaciation, widely known as "Snowball Earth" (Kirschvink 1992; Hoffman et al. 1998), in order to understand the causes of this global chilling. Was the cooling due to increased weathering and carbon sequestration due to (1) evolutionary advances in life on land (Hedges 2003); (2) evolutionary advances in marine life (Tziperman et al. 2011), (3) continental drift into warm-humid, tropical regions (Hoffman and Schrag 2002; Hoffman and Li 2009), or (4) large amounts of easily weatherable materials or aerosols produced by volcanism (Donnadieu et al. 2004; MacDonald and Wordsworth, 2017; Stern and Miller 2018; Long et al. 2019; Arnscheidt and Rothman 2020)? Other sections should also be evaluated for all four hypotheses, but this paper makes a start with the Chuar Group.

2. Geological background

The Tonian, Chuar Group of the Grand Canyon, Arizona (Fig. 1) accumulated within a rift basin on the western margin of North America (Fig. 2; Li et al. 2013; Eyster et al., 2020). The Chuar Group is 1622 m of gently folded shale, with thin beds of sandstone and stromatolitic dolomite (Fig. 3-4). A volcanic ash near the top of the sequence (1620 m in Fig. 5) has been dated from ^{206}Pb—^{238}U on zircon at 729 ± 9 Ma (Karlstrom et al. 2000; Rooney et al. 2018), preceding 717 Ma global advance of the first of the Neoproterozoic Snowball Earth glaciations (Kirschvink 1992; Hoffman et al. 1998). The Chuar Group is also unconformably below the Sixtymile Formation, now regarded as part of the Cambrian (508–499 Ma) Tonto Group (Karlstrom et al. 2018, 2020). A Re—Os age of 751 ± 0.9 Ma comes from marcasite nodules of the black shale near the base of the Awatubi Member (1150 m in Fig. 1) of the Chuar Group (Rooney et al. 2018). Detrital zircon ^{206}Pb—^{238}U maximum ages by CA-ID-TIMS in the Nankoweap Formation (−41 and − 77 m in Fig. 5) are 774.99 ± 1.54 Ma and 776.04 ± 0.98 Ma (Bullard 2018), and this formation is now included in the Chuar Group (Dehler et al. 2017). These various tie points give a linear model for age (M in Ma) from stratigraphic level (L in m) as follows ($R^2 = 0.95$).

$$M = -0.026L + 775.1 \text{ eq. (1)}.$$

Paleoenvironmental interpretations of the Chuar Group have evolved over the years (Table 1). The Chuar Group was originally conceived as deposits of coastal plains (Ford and Breed 1973; Vidal and Knoll 1983; Horodyski 1993) and lakes (Reynolds and Elston 1986; Reynolds et al. 1988; Cook 1991). In a break with the past, Dehler et al. (2001, p. 481) wrote, "All Chuar facies are consistent with a marine setting and there is no unequivocal evidence of terrestrial deposition in any facies (eg., lacustrine and alluvial deposits, paleosols". This interpretation was later modified. "Thicker intervals of carbonate facies with abundant exposure surfaces reflect restricted conditions, and local red beds may indicate stabilized land surfaces" (Dehler et al. 2017, l. 610). This is the position taken here, in which gray shales and dolostones of the Chuar Group are considered shallow marine to intertidal, but the red variegated mudrock facies was sampled and re-evaluated for paleosols (Table 1).

The paleoenvironmental relevance of fossils in the Chuar Group is uncertain, because the most common fossils, such as acritarchs (Vidal and Knoll 1983; Horodyski and Bloeser 1983; Vidal and Ford 1985) and *Chuaria* (Ford and Breed 1977), are of unknown biological affinities and
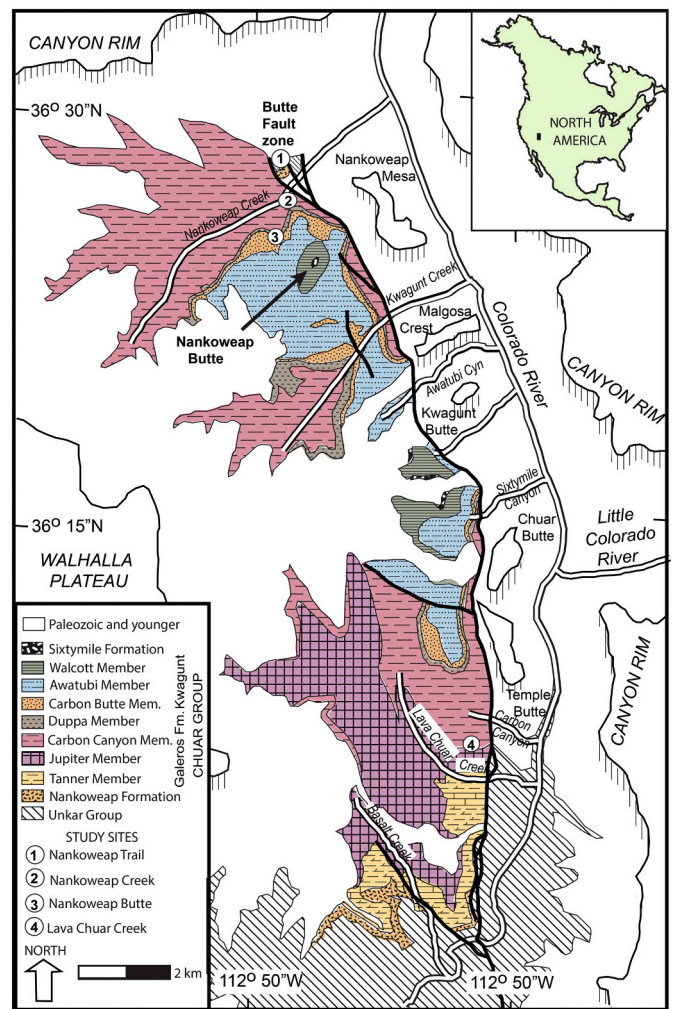

Fig. 1. Geological map of the Chuar Group of the eastern Grand Canyon, Arizona (after Dehler et al. 2005). Study sites are at stratigraphic levels shown in Fig. 5.

long extinct. One argument that they are marine is discovery of similar fossils of comparable age around the world (Johnston et al. 2010, Porter 2016; Porter and Riedman 2016; Dehler et al. 2017), but then modern lacustrine biota is surprisingly similar all around the world (Abell et al. 2008). Stromatolites are both marine and freshwater now (Cockbain 1976; Wacey et al. 2018), and in the past (Corkeron et al. 2012; Coffey et al. 2013). Fossil testate amoebae such as *Melanocyrillium* were found in nodules within pisolites and shales that are interpreted as aquatic (Table 1), but living relatives are now soil protists (Bloeser 1985; Porter and Knoll 2000; Porter et al. 2003). Biomarkers extracted from the Chuar Group show declining pristine/phytane ratios, 25–28-bisnorgammacerane and alkane-kerogen δ^{13}C, but increasing C^{27} cholestane up section, indicating a decline in cyanobacteria, but rise in algae, fungi, or metazoa within the upper Awatubi Member (van Maldegem et al. 2019).

Paleomagnetic data (Fig. 2B) indicates that the Chuar Group was deposited in a variety of temperate to tropical paleolatitudes from 64°N during deposition of the Jupiter Formation to as low as 10°N during deposition of the Walcott Member (Weil et al. 2004; Eyster et al. 2020), on the northwestern margin of Laurentia (Li et al. 2013). Paleolatitudes were calculated from data of Weil et al. (2004) to find paleopoles by the method of Butler (1992), and then paleolatitude by spherical trigonometry (Haile 1975). Other localities of comparable Tonian age with marine fossils collected as part of this work, and also studied geochemically (Retallack 2020), are Horsethief Springs in California,
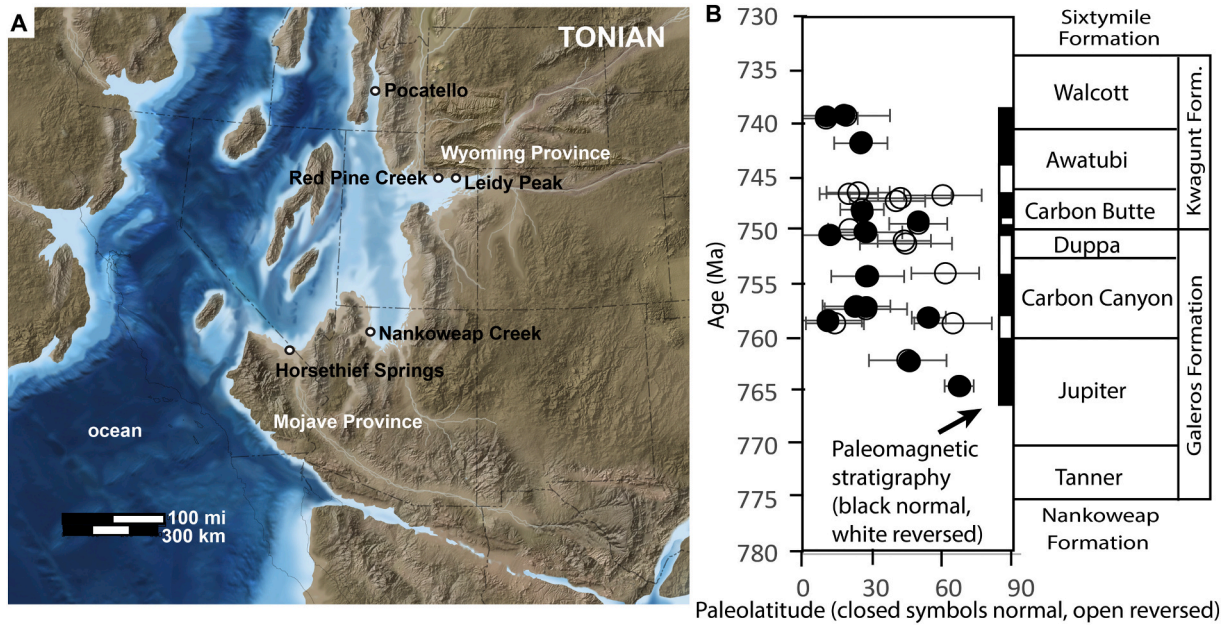
Fig. 2. Paleogeography (A) and paleolatitudes (B) of the Chuar Group; A, map courtesy of Ron Blakey (Colorado Plateau Geosystems Inc. license 70,920); B, paleolatitudes with α95 error calculated from data of Weil et al. (2004). Filled symbols are normal, and open symbols reversed. The age model is from radiometric dates (Rooney et al., 2016; Dehler et al. 2017; Bullard 2018), using eq. 1 in text.

Fig. 3. Overview of the Chuar Group in Nankoweap Creek, eastern Grand Canyon, Arizona from lower Nankoweap Trail.

Pocatello in Idaho, and both Red Pine Creek and Leidy Peak within the Uinta Mountains of Utah (Fig. 2A).

3. Materials and methods

Detailed sections for sampling were made of purple beds of the Tanner Member of the Galeros Formation along the Nankoweap Trail 1.2 km uphill from Nankoweap Creek at N36.287218° W111.896110°

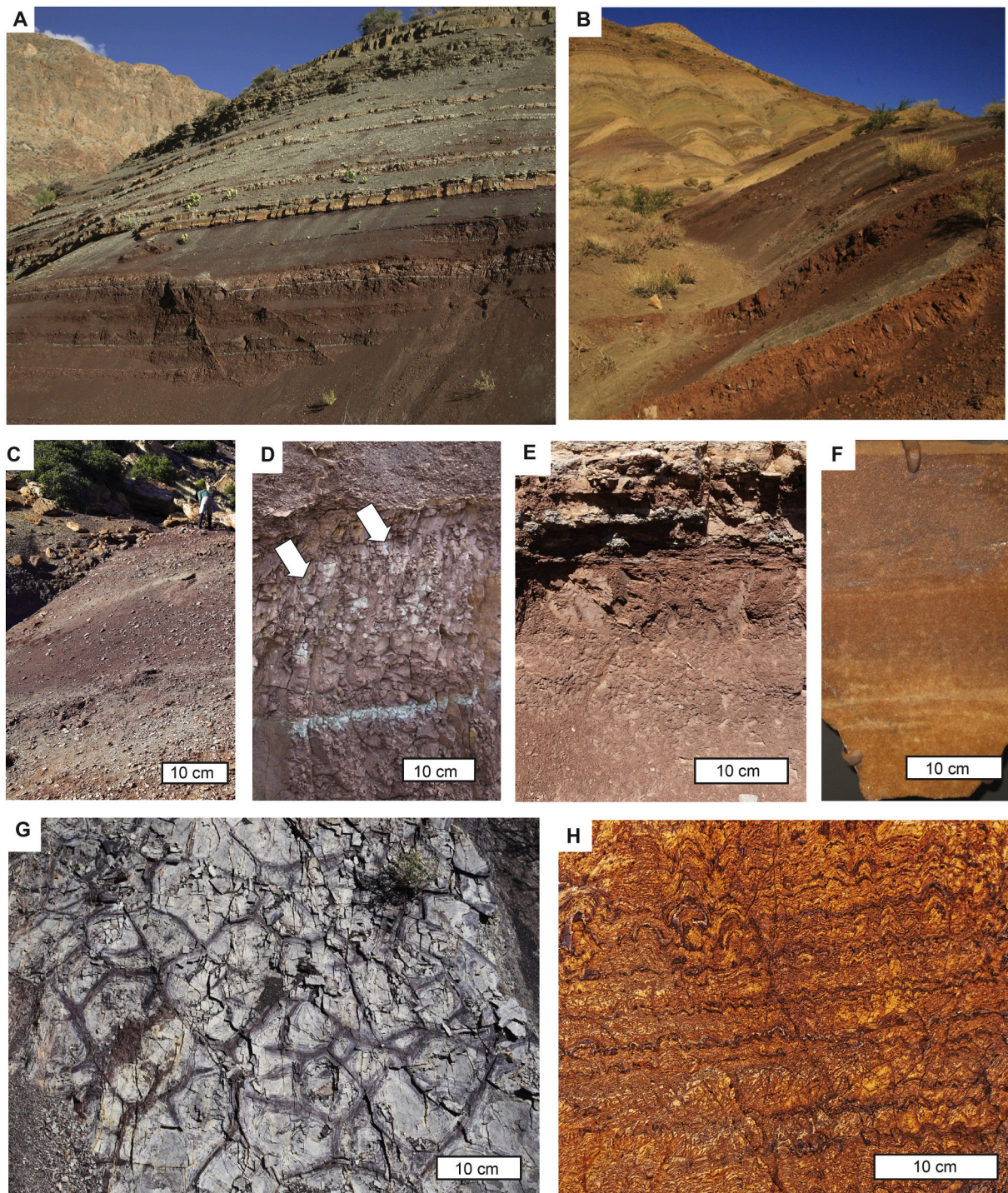**Fig. 4.** Field photographs of paleosols in the Chuar Group, Grand Canyon, Arizona: A, red paleosols in the Carbon Canyon Member (640 m) in Nankoweap Creek (N36.279081° W111.89082°); B, red paleosols in Jupiter Member (360 m) in Lava Chuar Canyon (N36.146098° W111.89082°); C, purple paleosols in upper Tanner Member (175 m) along Nankoweap Trail (N36.29424° W111.831805°); D, type Sekawa paleosol in Carbon Canyon Member Nankoweap Creek (same as panel A), with drab-haloed threads (*Prasinema*) at arrows; E, Sukwate paleosol in Carbon Butte Member (1046 m) below Nankoweap Butte (N36.268705° W111.89472°); F, Ematsile paleosol in lower Carbon Butte Member (1030 m same as panel E); G, desiccation cracks in the lower Carbon Canyon Formation (575 m) in Lava Chuar Canyon (N36.153296° W111.830886°); H, ferruginized and cracked stromatolites (*Inzeria inta*) from the basal Jupiter Member (187 m) along the lower Nankoweap Trail (N36.285518° W111.896266°). Stratigraphic levels are from Dehler et al. (2005, 2017). Panels D and E show green seams and filaments from burial gleization (Retallack 2019), and *Prasinema* (Retallack, 2011), respectively. Panels B,G with permission of Wayne Ranney, and panel E from Paul Strother. (For interpretation of the references to color in this figure legend, the reader is referred to the web version of this article.)
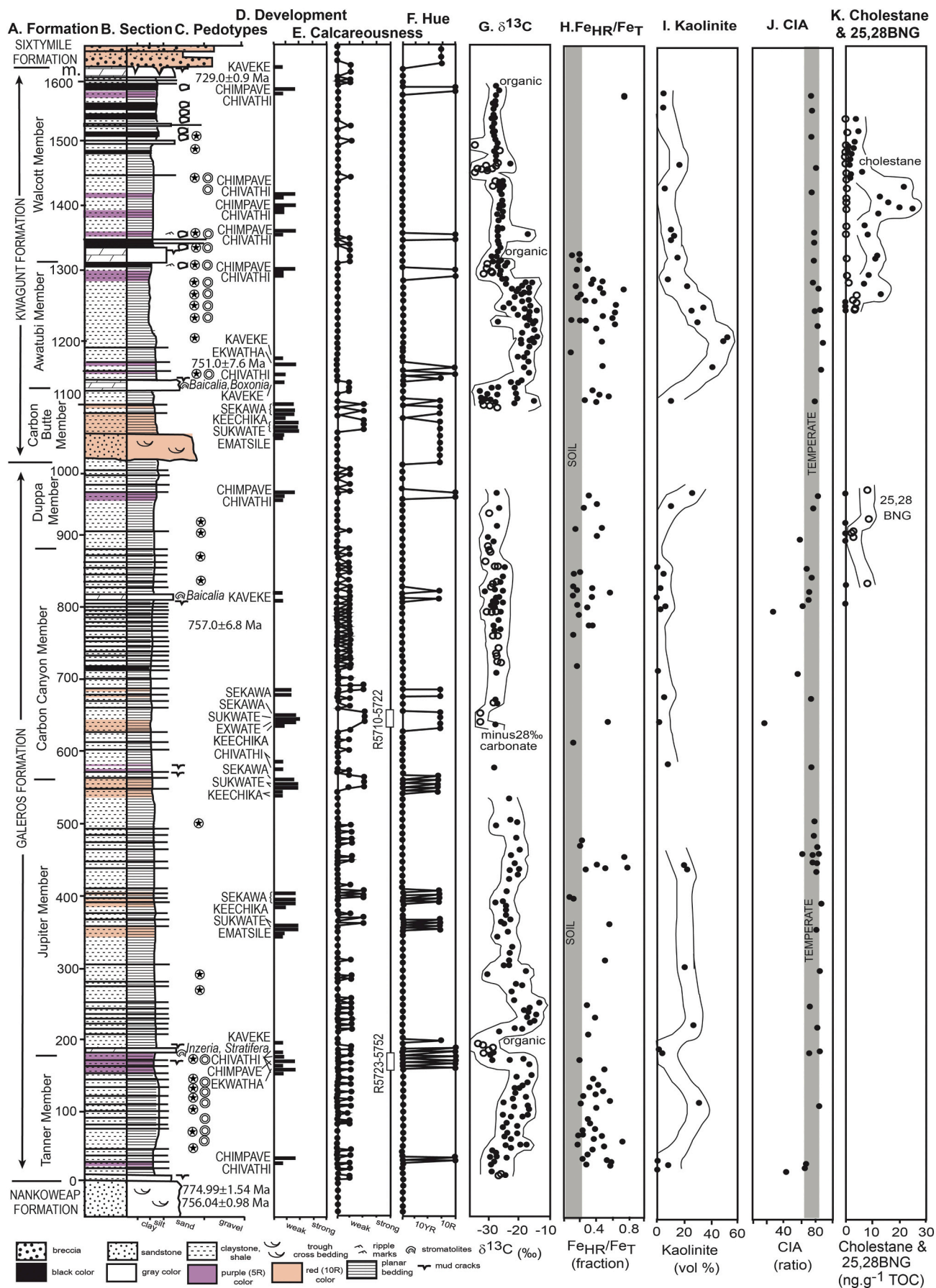
(caption on next page)

Fig. 5. Geological section and chemical data of the Chuar Group in the Grand Canyon, Arizona: A-B, formations, geological section, fossils, and radiometric ages (Dehler et al. 2005, 2017; Rooney et al., 2016; Bullard 2018) C-D, paleosol types (herein); E, paleosol development (scale of Retallack 2019); F, scale of reaction with dilute HCl (scale of Retallack 2019); G, Munsell Hue with distinct purple (5R) and red (10R) paleosols; G, $\delta^{13}C$ of organic matter (closed symbols) and of carbonate (open symbols) minus 28‰ to align it with organic values (after Dehler et al. 2017); H, degree of oxidation (Fe_{HR}/Fe_T) with shaded area < 0.2 of modern well drained soils (Johnston et al. 2010); I, percent kaolinite (Dehler et al. 2005), J, Chemical Index of Alteration (CIA) with temperate paleoclimatic range (70–85%) shaded (Dehler et al. 2005); K, C27 cholestane (closed symbols) and 25,28 bisnorgammacerane (open symbols) for upper part of section (van Maldegem et al. 2019). (For interpretation of the references to color in this figure legend, the reader is referred to the web version of this article.)

Table 1
Sedimentary facies and interpretations of the Chuar Group.

Facies	Interpretations of Dehler et al. (2001)	Interpretation Dehler et al. (2017), herein
Dark mudrock	Subtidal to intertidal marine low energy	Subtidal to intertidal marine low energy
Variegated mudrock	Subtidal to intertidal marine low energy	Coastal plain paleosols low energy
Laminated and cross-bedded sandstone	Subtidal to intertidal marine high energy	Coastal plain beach ridges high energy
Large-scale cross-bedded sandstone	Shallow subtidal marine high energy	Coastal plain paleochannels high energy
Laminated dolomite	Shallow subtidal to supratidal marine	Shallow subtidal to supratidal marine
Massive dolomite	Intertidal to supratidal marine	Intertidal to supratidal marine
Stromatolitic buildup	Shallow subtidal to intertidal marine	Shallow subtidal to intertidal marine
Oolitic-pisolitic grainstone	High energy beach and subtidal bars	High energy beach and subtidal bars
Coarse dolomite	Shallow subtidal channels and sand waves	Shallow subtidal channels and sand waves

(Fig. 4C), and of red beds of the Carbon Canyon Member of the Galeros Formation along Nankoweap Creek 1.1 km upstream of the narrow gorge to the Colorado River at N36.279293° W111.89076° (Figs. 4A, D). Also examined were red beds of the Jupiter Member of the Galeros Formation in the saddle between Carbon and Lava Chuar Canyon 1 km west of the Colorado River at N36.146098° W111.831805° (Fig. 4B), and Carbon Butte Member of the Kwagunt Formation, 1.1 km northwest of Nankoweap Butte at N36.268916° W111.894667° (Fig. 4E-F). Oriented rock samples were collected and archived in the Museum of Natural and Cultural History of the University of Oregon, and used for a variety of laboratory studies, including bulk chemical composition (Table 2). Thin sections were used to quantify grain size (Table 3) and mineral compositions (Table 4) by point counting (500 points) using a Swift automated stage and Hacker counting box on a Leitz Orthoplan Pol research microscope. Accuracy of such point counts is ±2% for common constituents (Murphy 1983). Major and trace element chemical analysis was determined by XRF from fused beads at ALS Chemex in Vancouver, Canada, with errors also in Table 2 from multiple analyses of standard granodiorite. Bulk density was measured by the clod method (Retallack 2019): from raw weight, then clods coated in paraffin of known density (0.86 g.cm^{-3}) in and out of chilled (6 °C) water (1.00 g.cm^{-3}). Stable isotopic compositions ($\delta^{18}O$ and $\delta^{13}C$) of carbonate nodules in the Sekawa profile were determined as low-magnesium calcite using Gasbench II and 10-kV Finnigan MAT 253 mass spectrometer in the

Table 2
Major element chemical composition (wt%) from XRF of samples from the Chuar Group, Arizona.

Pedotype	Specimen	SiO₂	TiO₂	Al₂O₃	Fe₂O₃	FeO	CaO	MgO	Na₂O	K₂O	MnO	P₂O₅	SrO	BaO	LOI	Total	g/cc
above Sekawa	R5710	35.27	0.54	9.17	4.85	1.77	10.69	14.07	0.57	1.82	0.19	0.108	0.05	0.77	21	99.11	2.5128
Sekawa	R5711	41.84	0.62	10.98	4.24	1.31	7.49	13.44	0.7	2.18	0.11	0.162	0.01	0.03	17.2	99	2.6283
Sekawa	R5712	40.5	0.53	9.43	3.09	0.91	9.99	12.94	0.58	2.1	0.15	0.138	0.01	0.04	19.85	99.35	2.6046
Sekawa	R5713	40.68	0.5	9.09	2.91	0.91	10.47	12.77	0.56	2.06	0.15	0.13	0.01	0.03	20.2	99.56	2.6146
Sekawa	R5714	63.69	0.67	13.4	3.93	1.11	0.59	6.54	0.75	3.62	0.02	0.115	0.01	0.04	6.73	100.1	2.5024
Sukwate	R5715	61.54	0.65	13.27	6.55	1.01	0.49	6.57	0.64	3.56	0.03	0.074	0.02	0.12	6.76	100.3	2.5332
Sukwate	R5716	62.58	0.67	12.96	6.51	0.98	0.21	6.11	0.73	3.53	0.01	0.071	0.01	0.06	6.07	99.53	2.5618
Sukwate	R5717	59.47	0.72	13.43	6.5	1.11	0.22	8.41	0.9	3.15	0.01	0.074	0.01	0.06	6.72	99.67	2.5692
Sukwate	R5718	57.34	0.74	13.53	6.62	1.34	0.22	10.31	0.92	2.78	0.02	0.075	0.01	0.05	7.31	99.94	2.5462
Sukwate	R5719	57.02	0.63	13.3	6.23	1.31	0.23	10.33	0.89	2.73	0.02	0.073	0.01	0.05	7.36	98.98	2.5386
Exwate	R5720	51.51	0.76	13.44	6.46	1.51	1.32	13	0.83	2.39	0.03	0.095	0.01	0.05	9.72	99.62	2.5338
Exwate	R5721	57.41	0.74	13.16	5.88	1.41	1.22	10.94	0.92	2.59	0.01	0.073	0.01	0.05	7.42	99.43	2.5388
Exwate	R5722	43.92	0.69	12.53	5.91	1.4	4.56	14.48	0.64	2.16	0.1	0.091	0.02	0.15	14.35	99.61	2.6755
Chivathi	R5723	88.37	0.55	3.85	1.42	0.39	0.08	0.51	0.04	1.03	<0.01	0.025	0.04	1.8	1.39	99.12	2.5628
Chivathi	R5724	67.98	1.12	13.20	8.83	0.79	0.07	0.99	0.04	3.88	0.01	0.07	0.03	0.04	3.68	100.05	2.6632
Chivathi	R5725	61.97	1.26	14.53	12.67	0.69	0.06	0.56	0.04	4.36	0.01	0.076	0.03	0.05	3.83	99.45	2.6608
Chivathi	R5726	60.1	1.18	15.99	12.86	0.82	0.07	0.6	0.03	4.77	0.01	0.088	0.03	0.03	4.07	99.84	2.6987
Chivathi	R5727	59.97	1.21	16.12	12.74	0.85	0.08	0.57	0.03	4.81	0.01	0.088	0.03	0.03	4.08	99.78	2.5061
Chimpave	R5728	73.96	1.03	10.5	7.61	0.62	0.07	0.38	0.02	3.1	0.01	0.049	0.02	0.05	2.65	99.45	2.5993
Chimpave	R5729	73.08	0.98	10.65	8.71	0.62	0.07	0.35	0.03	3.14	0.01	0.051	0.02	0.05	2.7	99.84	2.8895
Chimpave	R5730	61.84	1.26	17.45	8.99	0.65	0.1	0.56	0.03	5.14	0.01	0.072	0.03	0.02	4.27	99.78	2.8895
Chimpave	R5732	66.84	1.15	16.99	5.33	0.52	0.08	0.54	0.03	4.73	0.01	0.061	0.02	0.1	4.28	100.15	2.5470
Chimpave	R5733	67.79	1.11	16.15	4.93	0.49	0.08	0.53	0.03	4.53	0.01	0.056	0.02	0.11	4.11	99.47	2.4797
Chimpave	R5734	68.65	1.1	13.04	9.34	0.39	0.06	0.41	0.03	3.65	<0.01	0.066	0.02	0.21	3.32	99.91	2.5649
Chimpave	R5735	70.63	1.06	13.00	6.7	0.39	0.07	0.42	0.02	3.64	<0.01	0.066	0.02	0.27	3.43	99.34	2.4992
Ekwatha	R5746	68.99	1.06	17.04	1.86	0.49	0.07	0.59	0.03	4.8	<0.01	0.065	0.02	0.02	4.4	98.96	2.5509
Ekwatha	R5747	66.37	1.08	15.11	7.11	0.85	0.05	0.54	0.03	4.6	0.01	0.057	0.01	0.03	4.01	99.02	2.6117
Ekwatha	R5749	57.28	0.96	13.18	19.22	0.82	0.04	0.48	0.02	4.03	<0.01	0.047	0.01	0.02	4.06	99.36	2.5774
Ekwatha	R5750	62.57	0.87	14.28	11.42	0.69	0.05	0.44	0.02	4.23	0.01	0.049	0.01	0.07	5.29	99.32	2.4297
Ekwatha	R5751	73.09	1.03	14.44	2.49	0.49	0.03	0.44	0.02	4.17	<0.01	0.056	0.01	0.02	3.99	99.8	2.4046
Ekwatha	R5752	74.78	0.94	13.4	1.95	0.46	0.04	0.41	0.02	3.82	<0.01	0.054	0.01	0.06	3.5	98.98	2.0993
Error	all	2.705	0.06	0.825	0.395			0.22	0.18	0.11	0.13	0.025	0.030			0.35	0.02

Note: Errors are from 10 replicate analyses of the standard, CANMET SDMS2 (British Columbia granodioritic sand).

Table 3

Grain-size data from point counting thin sections (500 points) of samples from the Chuar Group, Arizona.

Pedotype	Hoz	No.	% sand	% silt	% clay	Textural class	Grain fabric	Plasmic fabric
above	above	R5710	19.2	52.6	28.2	silty clay loam	porphyroskelic	calciasepic
Sekawa	A	R5711	6.8	57.6	35.6	silty clay loam	porphyroskelic	insepic
Sekawa	Bk	R5712	9.8	64.6	25.6	silt loam	porphyroskelic	mosepic
Sekawa	Bk	R5713	7.4	67.8	24.8	silt loam	porphyroskelic	mosepic
Sekawa	C	R5714	39.4	38.8	21.8	loam	agglomeroplasmic	skelsepic
Sukwate	A	R5715	33.4	39.8	26.8	loam	agglomeroplasmic	skelmosepic
Sukwate	A	R5716	29.0	44.2	26.8	loam	agglomeroplasmic	skelmosepic
Sukwate	Bk	R5717	28.0	47.2	24.8	loam	agglomeroplasmic	skelmosepic
Sukwate	Bk	R5718	18.6	57.4	24.0	silt loam	agglomeroplasmic	insepic
Sukwate	C	R5719	11.8	64.4	23.8	silt loam	agglomeroplasmic	insepic
Exwate	A	R5720	11.0	56.8	32.2	silty clay loam	agglomeroplasmic	bimasepic
Exwate	Bw	R5721	15.4	61.0	23.6	silt loam	agglomeroplasmic	bimasepic
Exwate	C	R5722	31.2	46.6	22.2	silt loam	agglomeroplasmic	insepic
above	above	R5723	27.8	55.8	16.4	silt loam	granular	silasepic
Chivathi	A	R5724	20.8	48.4	30.2	clay loam	porphyroskelic	clinobimasepic
Chivathi	Bg	R5725	20.6	47.4	32.0	clay loam	porphyroskelic	argillasepic
Chivathi	Bg	R5726	27.8	48.8	23.4	loam	agglomeroplasmic	isotic
Chivathi	C	R5727	35.4	40.2	24.4	loam	agglomeroplasmic	insepic
Chimpave	A	R5728	11.8	72.0	16.2	silt loam	porphyroskelic	isotic
Chimpave	C	R5729	15.2	63.8	21.0	silt loam	porphyroskelic	argillasepic
Chimpave	C	R5730	4.8	63.0	32.2	silty clay loam	agglomeroplasmic	argillasepic
Chimpave	A	R5732	10.8	70.6	18.6	silt loam	agglomeroplasmic	skelmosepic
Chimpave	C	R5733	10.6	60.8	28.6	silty clay loam	agglomeroplasmic	skelmosepic
Chimpave	C	R5734	14.2	54.6	31.2	silty clay loam	agglomeroplasmic	skelmosepic
Chimpave	C	R5735	17.0	67.6	15.4	silt loam	agglomeroplasmic	argillasepic
above	above	R5736	10.4	59.4	30.2	silty clay loam	agglomeroplasmic	argillasepic
Chimpave	A	R5737	11.0	67.0	22.0	silt loam	agglomeroplasmic	skelmosepic
Chimpave	C	R5738	17.2	61.4	21.4	silt loam	agglomeroplasmic	skelmosepic
Chimpave	A	R5739	15.4	65.2	19.4	silt loam	agglomeroplasmic	skelmosepic
Chimpave	C	R5740	9.2	71.4	19.4	silt loam	agglomeroplasmic	argillasepic
above	above	R5746	14.8	59.8	25.4	silt loam	porphyroskelic	argillasepic
Ekwatha	A	R5747	13.8	53.0	33.2	silty clay loam	porphyroskelic	skelmosepic
Ekwatha	By	R5748	17.4	62.8	19.8	silt loam	porphyroskelic	skelmosepic
Ekwatha	By	R5749	21.8	57.8	20.4	silt loam	agglomeroplasmic	isotic
Ekwatha	By	R5750	16.4	59.4	24.5	silt loam	intertextic	argillasepic
Ekwatha	C	R5751	25.2	46.8	28.0	clay loam	porphyroskelic	mosepic
Ekwatha	C	R5752	19.4	51.8	28.8	silty clay loam	porphyroskelic	argillasepic

University of Oregon laboratory of Ilya Bindeman (Table 5), supplementing large datasets of isotopic data for the Chuar Group published by Dehler et al. (2005, 2017) and Johnston et al. (2010). Silica-filled microfossils were macerated from the red beds using concentrated HF, and neutralizing with sodium hydroxide, then mounting on metal stubs for examination in the QANTA environmental Scanning Electron Microscope in the CAMCOR analytical laboratories of the University of Oregon.

4. Metamorphic and diagenetic alteration

The formation of soil on sediment is a type of early diagenetic alteration, which can be reconstructed after consideration of additional late diagenetic and metamorphic alteration. The Chuar Group of the Grand Canyon shows three early diagenetic features common in red beds: (1) drab mottles in upper portions of beds due to burial gleization of buried organic matter, (2) dark red (Munsell 10R-5R) color from dehydration reddening of ferric hydroxide minerals, and (3) substantial lithostatic compaction (Retallack 2019). Burial gleization is chemical reduction of oxides and hydroxides of iron by anaerobic bacteria on subsidence into anoxic water usually resulting from rapid burial, and is especially suggested by drab mottles and tubular features radiating down from bed tops (Fig. 4D), as in Cambrian (Álvaro et al. 2003; Retallack 2008) and Proterozoic red beds (Driese et al. 1995; Retallack 2016b). Geologically ancient red beds are also purple to red in color from burial dehydration of ferric oxyhydroxides (Fig. 4A-B), unlike brown to yellow modern soils and late Pleistocene sediments (Retallack 2019). The difference between the Chuar Group purple beds (Fig. 4C, G) and red beds (Figs. 4A-B, E-F) is organic matter: 0.14–0.48 wt% organic C in red (10R Munsell hue) beds, but 0.57–3.51 wt% organic carbon (C)

in purple (5R Munsell hue) beds. These red and purple beds are organic lean, but black shale in the Chuar Group (Fig. 5) has 1.42–9.39 wt% organic C (Dehler et al. 2017). All the Chuar Group kerogen analyzed by Dehler et al. (2005) has the light isotopic composition (−15.73 to −29.91‰ vs VPDB) of photosynthetically produced organic carbon.

The Chuar Group is folded into a meridional syncline truncated to the east by the Butte Fault (Ford and Breed 1973). Illite crystallinity values are 0.9–1.5° 2θ in overlying Cambrian rocks, which would have seen burial temperatures not much more than 100 °C although buried by at least 2.6 km of overburden (Verdel et al. 2011). Adding 61 m for the Sixtymile Formation (Elston 1979), also of Cambrian age (Karlstrom et al. 2020), gives observed overburden to the Chuar Group as 2.7 km, but total overburden at the base of the group is as thick as 4.2 km. Assessment of thermal maturity of organic matter by Rock-Eval pyrolysis in the Chuar Group indicates maximum temperatures of no more than 379–445 °C (Wiley et al. 2001; Van Maldegem et al., 2019). Sterane/hopane ratios and total organic carbon of Nankoweap Butte samples suggest thermal maturity within the late oil window, typically at 50-150 °C burial temperature (Zumberge et al., 2019). With highly variable potash values of 0.51 to 7.31 wt% (Table 1), there is evidence of local, but not pervasive potash metasomatism (Novoselov and de Sousa Filho 2015). Burial compaction (C as %) expected for 2.7–4.2 km burial can be calculated as 62% at the top of the Chuar Group and 57% at the base. These calculations use the following formula (eq. 2) with depth of burial (B in km) and 0.51, 0.49, and 0.27 as physical constants (of Sheldon and Retallack 2001). Such compaction estimates are needed for paleoenvironmental interpretations from bed thicknesses (Retallack 2019).

$$C = \frac{-0.51 \times 100}{\left\{ \left(\frac{0.49}{e^{\frac{B}{0.27}}} \right) - 1 \right\}} \text{ eq. (2).}$$

Table 4

Mineral content from point counting thin sections (500 points) of samples from the Chuar Group, Arizona.

Pedotype	Hoz	No.	% clay	% gypsum	% calcite	% rock	% feldspar	% mica	% quartz	% opaque
above	above	R5710	28.6	0	27.0	1.4	20.6	1.4	17.4	3.6
Sekawa	A	R5711	36.2	0	3.2	1.4	30.0	1.6	23.2	4.4
Sekawa	Bk	R5712	24.0	0	27.2	2.4	23.6	0.4	20.8	1.6
Sekawa	Bk	R5713	26.4	0	24.2	2.2	22.6	0.6	22.2	1.8
Sekawa	C	R5714	22.3	0	0	12.6	33.0	0.6	28.2	3.4
Sukwate	A	R5715	28.2	0	3.4	4.0	30.4	0.4	30.2	3.4
Sukwate	A	R5716	26.6	0	1.4	5.0	30.6	2.8	27.8	5.8
Sukwate	Bk	R5717	25.8	0	5.4	4.0	31.8	1.6	26.6	4.8
Sukwate	Bk	R5718	25.0	0	4.2	4.4	30.8	3.8	28.4	3.4
Sukwate	C	R5719	24.2	0	1.0	5.6	33.4	4.2	27.6	4.0
Exwate	A	R5720	31.6	0	0	5.0	30.2	4.6	24.0	4.0
Exwate	Bw	R5721	22.8	0	0	6.2	34.0	6.6	27.6	2.8
Exwate	C	R5722	22.6	0	21.8	7.4	25.0	1.2	21.8	0.2
above	above	R5723	14.2	0	0	3.2	34.6	1.8	41.8	4.4
Chivathi	A	R5724	31.6	0	0	1.2	30.8	2.6	26.8	7.0
Chivathi	Bg	R5725	32.2	0	0	2.6	27.6	1.2	26.2	10.2
Chivathi	Bg	R5726	24.8	0	0	3.4	23.8	5.0	24.0	19.0
Chivathi	C	R5727	25.6	0	0	10.4	29.6	1.4	24.4	8.6
Chimpave	A	R5728	17.6	0	0	7.8	34.4	4.2	30.4	5.6
Chimpave	C	R5729	20.4	0	0	6.0	34.6	5.2	28.4	5.4
Chimpave	C	R5730	32.6	0	0	2.4	29.2	2.0	26.8	7.0
Chimpave	A	R5732	17.4	0	0	4.8	38.0	2.8	34.6	2.4
Chimpave	C	R5733	27.2	0	0	4.4	33.4	0.4	30.2	4.4
Chimpave	C	R5734	34.4	0	0	1.4	30.0	5.8	22.2	6.2
Chimpave	C	R5735	17.4	0	0	3.4	35.4	7.2	29.4	7.2
above	above	R5736	30.2	0	0	1.8	32.6	5.2	28.0	2.2
Chimpave	A	R5737	20.4	0	0	1.8	38.8	7.4	29.8	1.8
Chimpave	C	R5738	23.2	0	0	4.2	36.8	8.2	26.2	1.4
Chimpave	A	R5739	22.2	0	0	5.0	32.8	5.4	28.4	6.2
Chimpave	C	R5740	21.0	0	0	6.8	28.8	13.2	26.4	3.8
above	above	R5746	23.8	0	0	5.8	35.0	3.8	28.8	2.8
Ekwatha	A	R5747	33.8	0	0	2.2	27.6	5.4	23.0	8.0
Ekwatha	By	R5748	21.2	8.4	0	2.6	27.2	7.8	24.0	8.8
Ekwatha	By	R5749	23.4	5.4	0	1.2	30.6	6.0	28.4	5.0
Ekwatha	By	R5750	25.2	3.2	0	3.2	31.6	5.4	28.4	3.0
Ekwatha	C	R5751	28.4	3.2	0	2.0	31.6	0.8	30.2	3.8
Ekwatha	C	R5752	29.0	0	1.0	3.6	31.2	0.4	28.6	6.2

Table 5

New carbonate stable isotopic analyses estimates of Sekawa paleosol at 640 m.

Spec-imen	δ¹³C carbonate vs VPDB (‰)	δ¹⁸O carbonate vs VPDB (‰)
R5713A	−1.25 ± 0.03	−2.20 ± 0.04
R5713B	−1.18 ± 0.04	−1.90 ± 0.04
R5713C	−1.30 ± 0.05	−1.95 ± 0.12
R5713D	−1.43 ± 0.16	−3.00 ± 0.13
R5713E	−1.24 ± 0.07	−2.20 ± 0.10

Note: All analyses are calcite nodules from Sekawa paleosol analyzed at University of Oregon. Specimens are in collection of Museum of Natural and Cultural History, University of Oregon. Erros are statnadrd deviation of 3 analyses.

5. Paleosol recognition

Paleosols are definitively recognized in the field as horizons of fossil root traces (Retallack 2019), but rooted vascular land plants did not evolve until the Silurian (Retallack 2015a). Without root traces a variety of other features can be used to recognize paleosols in Precambrian nonmarine facies, such as soil cracking structures, pseudomorphs of soluble salts (Southgate 1986, 1989; Retallack 2016b), and molar weathering ratios (Nesbitt and Young 1982). The following paragraphs consider each of these paleosol criteria in turn.

5.1. Crack patterns

Cracks with the v-shaped profile of desiccation cracks in clay (Weinberger 2001) were seen at several levels in the Chuar Group (Fig. 4E, G; Dehler et al. 2001, Fig. 3A), including silt-filled cracks extending down into siltstone (Fig. 6A). These siltstone cracks emanate from the most hematite-rich tops of sandy beds, and the enigma of silt cracking like clay has been explained by Prave (2002) as due to abundant hydrated microbiota, like that of a microbial earth soil (Retallack 2012a). A spectacular case of a ptygmatically folded, white dolomicrite in gray dolostone of the polygonal marker bed is figured by Dehler et al. (2001, Fig. 3E). An alternative explanation may be frost cracking in a periglacial soil (Kokelj et al. 2007; Raffi and Stenni 2011), but ice wedges are more strongly tapering than Chuar mudcracks (Fig. 4F). Other alternatives in marine settings are syneresis cracks from flocculation of clays, but these are shallow and parallel sided rather than deep and v-shaped (Plummer and Gostin 1981).

Simple desiccation polygons are technically paleosols of very weak development (Entisols), but other soils have more complex cracks, revealed by surface modifications known as cutans (Retallack 2019). Sesquans (iron and aluminum-stained cracks) are ptygmatically folded by compaction to create a blocky angular pedal structure below the laminated cover to paleosols, apparent in the field (Fig. 4D, E), and also in vertically oriented thin sections (Fig. 6D). Marine or lacustrine shales in contrast have clear lamination or varves (Renaut and Tiercelin, 1994; Zillen et al. 2003). Lamination is clear within interbeds to the cracked pedal units of the Chuar Group (Fig. 6E).

5.2. Angular silt

Point counting of the variegated mudrock facies of the Chuar Group reveals abundant (29–72 vol% in Table 3), angular, silt-size grains (Fig. 7). These rocks are not the claystones they appear to be in hand specimen, but are mostly grain-supported angular silt grains, with scattered clasts of sand size (Fig. 5).

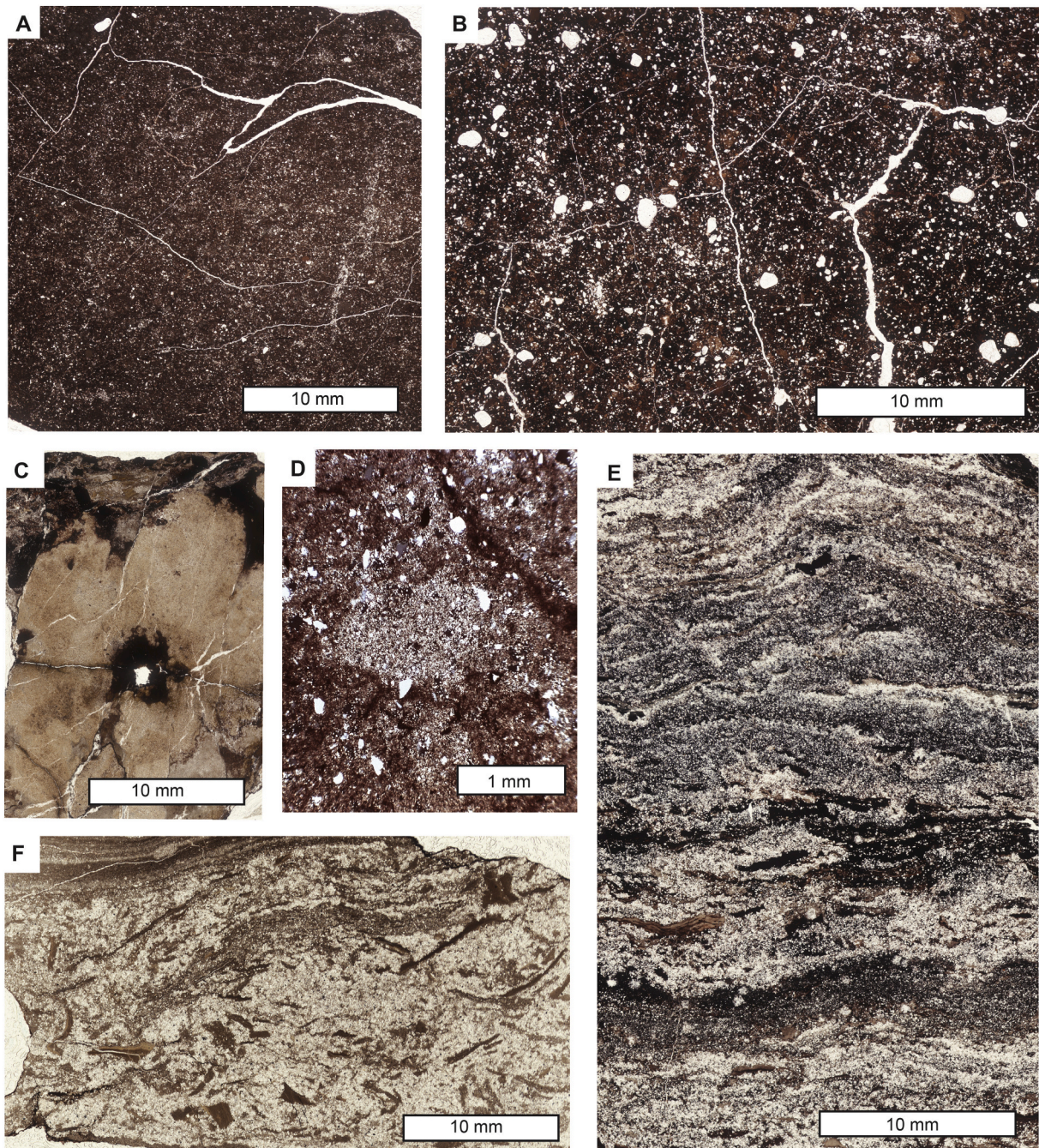These abundances and mineral compositions of Chuar Group red

Fig. 6. Thin sections of Chuar Group paleosols, all cut vertical to regional bedding; A, silt-filled cracks in red claystone A horizon of Sekawa pedotype (R5711); B, cracking and porphyroskelic skelmosepic fabric in A horizon of Sukwate pedotype (R5715); C, radial desert rose of gypsum in By horizon of Ekwatha pedotype (R5748); D, incipient micritic nodules in Bk horizon of Sekawa pedotype (R5713); E, disrupted lamination and brecciation in C horizon of Chimpave pedotype (R5728); F, red claystone clasts redeposited in gray sandstone of C horizon of Chimpave pedotype (R5746). (For interpretation of the references to color in this figure legend, the reader is referred to the web version of this article.)

beds are similar to Quaternary Peoria Silt, which is sandy in Nebraska but fine silt in Mississippi (Pye and Sherwin 1999). Peoria loess of Kansas and Nebraska is non-calcareous and volcaniclastic (Swineford and Frye 1951), like the potential purple paleosols of the Tanner Member (Ekwatha, Chivathi, Chimpave profiles of Fig. 7). Peoria Loess is calcareous in Illinois (Grimley et al. 1998), Indiana (Ruhe and Olson 1980), and Mississippi (Bettis et al. 2003), like red paleosols of the Carbon Canyon Member (Sekawa, Sukwate, Exwate and Keechika profiles of Fig. 7). These differences reflect proximity to Cordilleran volcanoes in Kansas and Nebraska, but proximity to freshly deglaciated Paleozoic limestones and dolostones from Illinois to Mississippi. While

much more eolian silt may have fallen into the sea before the advent of land plants, silt grains are supported by clay and carbonate in Cambrian marine rocks (Dalrymple et al. 1985), rather than grain-supported as in the Chuar Group (Fig. 6B). Red loessic siltstones of the Chuar Group in vertically oriented thin sections are massive (Fig. 6A-B), and lack lamination or varves found in intertidal or lacustrine interbeds in the same sequence (Fig. 6E).

5.3. Sand crystals

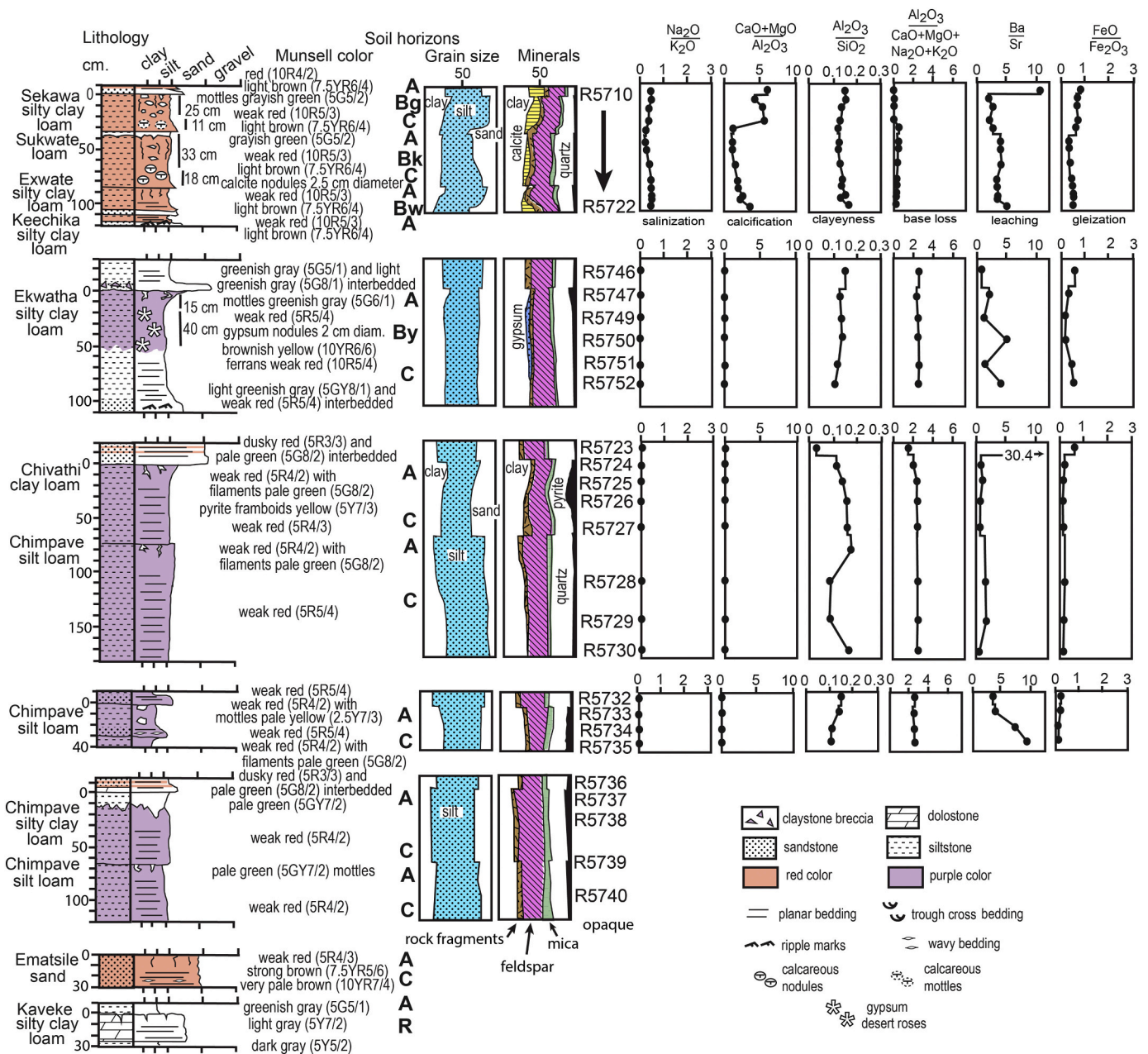Salt crystal casts in the Chuar Group have been recorded without

Fig. 7. Paleosol profiles of the Chuar Group, their petrographic composition from point counting thin sections, and weathering trends revealed by molecular weathering ratios (Tables 2-4). Location of these sections and specimens within the Chuar Group is shown in Fig. 5.

illustration by Ford and Breed (1973), Dehler et al. (2001), and van Maldegem et al. (2019). Limpid vein filling crystals of gypsum from laminated sediments of the upper Awatubi Member are illustrated by van Maldegem (2017, Fig. 6.3b). We found very different, scattered, 2-cm-diameter, sand crystals of radiating gypsum with abundant included quartz and feldspar grains scattered in purple claystone of the Ekwatha profile of the upper Tanner Member (Fig. 6C, 7).

These different forms represent very different paleoenvironments. Limpid crystals and seams of gypsum and anhydrite form in marginal marine or lacustrine sabkhas, where clear crystals precipitating from solution displace surrounding grains of saturated sediment (Renaut and Tiercelin, 1994; Ziegenbalg et al. 2010). Sand crystals on the other hand form by replacement and cementation without extensive displacement of matrix within the confining pressure of soil, and are known as "desert roses" (Watson 1985; Al Kofahi et al., 1993). As in gypsic horizons of desert soils (Retallack 2019), sand crystals are organized into subsurface

(By) horizons (Fig. 7). Gypsum accumulates below the most productive part of the soil (Breecker and Retallack 2014).

5.4. Calcareous nodules

Most carbonate in the Chuar Group is weakly effervescent dolomite, but testing in the field with dilute HCl and thin section observations found that red beds have common dispersed and nodular calcite (Fig. 7), amenable to stable isotopic analysis (Table 5). The effervescent patches proved to be low-magnesium calcite nodules, generally in the size range 3–4 mm (Fig. 6D), but sometimes coalescing into larger masses. Nodule margins are diffuse, and their micritic cement is replacive rather than displacive (Fig. 6D).

Low magnesium calcite nodules and mottles aggregated into sub-surface horizons (Fig. 7) are like calcic (Bk) horizons of soils (Retallack 2019). Marine or lacustrine dolostones of the Chuar Group on the other

hand are very different (Fig. 4H): dolomitic, gray to orange in color, well laminated within thick beds, and sometimes stromatolitic (Dehler et al. 2001, 2005). Most of the dolostones are gray and laminated, but some of the dolostones have reddened surfaces and irregular relief on top from exposure and dissolution in paleokarst (Fig. 7).

5.5. Mineral weathering trends

Point counting of individual red beds showed surface depletion of rock fragments and feldspar near the surface of some beds (Sekawa, Sukwate Chivathi and Exwate of Fig. 7), but not of others (Chimpave of Fig. 7). The beds lacking feldspar depletion all had abundant relict bedding. Clay enrichment toward the surface of the feldspar-depleted beds is abruptly truncated below sharp grain size discontinuities with overlying siltstone and sandstone, and clay is confined to intervals only 5–15 cm thick. Other gray graded beds of the Chuar Group, in contrast, had thick laminated upper portions below a basal sandstone (Fig. 4A).

Red and purple clayey bed tops do not have mineral composition like the upper part of graded beds deposited in a water column (Komar 1985; Korsch et al. 1993), for several reasons: little clay (no more than 36 vol %), no bedding, red or purple color, and loess-like silt abundance (Fig. 7). Asymmetric enrichment of clay in bed tops over intervals of only 15 cm is unlike symmetrical hydrothermal or diffuse metamorphic alteration (Kelka et al. 2017; Wallace and Hood 2018). A better explanation for the observations is clay formation by weathering of feldspar and rock fragments in beds massive because weathered for a long time (Figs. 6A-D), but not in beds showing little weathering from well preserved depositional bedding (Fig. 6E-F).

5.6. Chemical weathering trends

Chemical trends within the red and purple beds (Fig. 7) are very different from those of graded beds, which show surface enrichment in alumina, lime and magnesia (Korsch et al. 1993). In contrast, alumina to base ratios show segregation of alumina from alkaline earths in the upper part of the massive red profiles (Sekawa, Sukwate, Exwate of Fig. 7), but not in the purple profiles with relict bedding (Chivathi, Chimpave, Ekwatha of Fig. 7). The few sedimentary beds between the massive profiles have wildly different chemical composition (Fig. 7). The ratio of highly reactive iron to total iron (Fe_{HR}/Fe_T in Fig. 5H) may be another indication of paleosols when <0.2 (Johnston et al. 2010), which is a highly oxidized state found only in soils and not in marine sediments (Ku et al. 2008).

Alumina/silica molar ratios as a proxy for clayeyness are high near the surface of massive beds (Sekawa, Sukwate, Chivathi and Exwate of Fig. 7), but not in the well bedded units (Chivathi and Chimpave of Fig., 7). Ba/Sr molar ratios are evidence of chemical leaching, because Sr is more soluble than the other chemically similar element, and this ratio ranges from 1 to 10 in soils (Vinogradov 1959). Ba/Sr ratios are low or erratic in the Chuar Group. Low to modest soda/potash ratios, are evidence against soda enrichment (salinization) within beds (Fig. 7). Low ferrous/ferric iron confirms red and purple color from hematite as evidence of oxidizing conditions, but rising ratios in the base of two beds (Sekawa and Ekwatha of Fig. 7) may reflect chemical reduction (gleization) within groundwater (Vepraskas and Sprecher 1997). Oxidation and reduction during the Tonian, rather than in modern outcrop is indicated by close alternation of drab and red beds in outcrop (Fig. 2), and erosion and deposition of red clayey clasts within gray sandstone (Fig. 6F).

5.7. Tau analysis

A definitive method to disentangle soil formation from sedimentation is tau analysis (Brimhall et al. 1992). Tau analysis isolates two separate aspects of weathering: mole fraction mass transport ($\tau_{j,w}$) of a mobile element and mole fraction strain ($\varepsilon_{i,w}$) of an immobile element

(Ti used here), using the following formula including bulk density (ρ in g.cm^{-3}) and oxide assay (C in weight %) for successive samples (subscripts i,j) of weathered material (subscript w) and parent material (subscript p). The parent material in the case of a sedimentary bed is the material lower within the same bed, and in ancient sedimentary sequence pedogenic strain can be undone to some extent by compaction during deep burial.

$$\varepsilon_{i,w} = \left[\frac{\rho_p C_{j,p}}{\rho_w C_{j,w}}\right] - 1 \text{ eq. (3).}$$

$$\tau_{j,w} = \left[\frac{\rho_w C_{j,w}}{\rho_p C_{j,p}}\right] \left[\varepsilon_{i,w} + 1\right] - 1 \text{ eq. (4).}$$

Soils and paleosols lose mass with weathering and so have negative strain ($\varepsilon_{i,w} < 0$), and also lose nutrient cations and silica, so have negative mass transfer ($\tau_{j,w} < 0$). Thus soils and paleosols fall in the lower left quadrat of collapse and loss in a strain versus mass transfer plot (Fig. 8). In contrast, sediment accumulation and diagenetic alteration adds elements and mass so has positive strain and mass transfer and falls in the upper quadrats. Tau analysis has been widely used for Precambrian paleosols (Driese 2004; Liivämagi et al., 2014), as well as Cenozoic paleosols (Bestland et al. 1996; Sheldon and Tabor 2013), and modern soils (Chadwick et al., 1990; Hayes et al. 2019).

From the perspective of tau analysis, the analyzed beds of the Chuar Group are largely in the soil formation quadrat of collapse and loss (Fig. 8A). Once again massive red profiles (Sukwate, Sekawa, and Ekwate) show a greater mole fraction depletion than purple profiles with relict bedding (Chivathi, Ekwatha, and Chimpave profiles of Fig. 8A). Mass loss of elements plotted against depth within the beds shows little change in some paleosols, but chemical differentiation between horizons in the Sukwate and Ekwatha profiles are indicated by dashed lines (Fig. 8B). They do not show basal accumulation of the stable marker (Ti) in heavy minerals like ilmenite, which settle to the base of beds, and thus show positive strain ($\varepsilon_{i,w}$) in sedimentary turbidites and tempestites (Retallack 2016a).

5.8. 6.8. Stable isotopic covariance

Cross-plots of $\delta^{13}C$ and $\delta^{18}O$ in carbonate are useful paleoenvironmental indicators, because covariance is strong in calcareous nodules of Holocene soils (Fig. 9B) in China (Huang et al. 2005) and Arizona (Knauth et al. 2003). Less statistically significant correlations (Fig. 9C-D) are found in soil carbonate crusts (Knauth et al. 2003), and marine limestone altered by deep circulation of meteoric water (Lohmann 1988; Melim et al. 2004). Lake carbonates with covariant stable isotopes may also be a case of meteoric alteration, because only found in seasonally dry lakes, not perennial open system lakes (Talbot 1990). In contrast, unaltered marine limestones and sea shells (Fig. 9E) show no hint of correlation (Surge et al. 1997; Veizer et al. 1999). Near constant $\delta^{18}O$ but highly varied $\delta^{13}C$ (Fig. 9F) is created by microbial methanogenesis in carbonate of marine methane seeps (Aiello et al. 2001; Peckmann et al. 2002), and siderite of wetland paleosols (Ludvigson et al. 1998, 2013).

Pedogenic, highly correlated C and O isotopic patterns were observed in pedogenic nodules of red beds (Sekawa profile) and a cracked dolostone bed (Kaveke), but there is no correlation for stromatolitic and other presumed marine dolostones of the Chuar Group. which vary widely (crosses of Fig. 9). Correlations of $\delta^{13}C$ and $\delta^{18}O$ are not accidental, but due to selection for light isotopologues of CO_2 in soils, unlike the sea or lakes with oxygen of water vastly in excess of carbon (Farquhar and Cernusak 2012). Correlation in post-Silurian soils is related to stomatal conductance and fractionation by photosynthetic enzymes such as rubisco (Retallack 2016b) and carbonic anhydrase (Chen et al. 2018), because $\delta^{13}C$ and $\delta^{18}O$ covariance is seen in respired soil CO_2 (Ehleringer and Cook 1998; Ehleringer et al. 2000), and in plant cellulose (Barbour and Farquhar 2000; Barbour et al. 2002). A role for stomates is undermined by correlation of $\delta^{13}C$ and $\delta^{18}O$ in Ordovician,
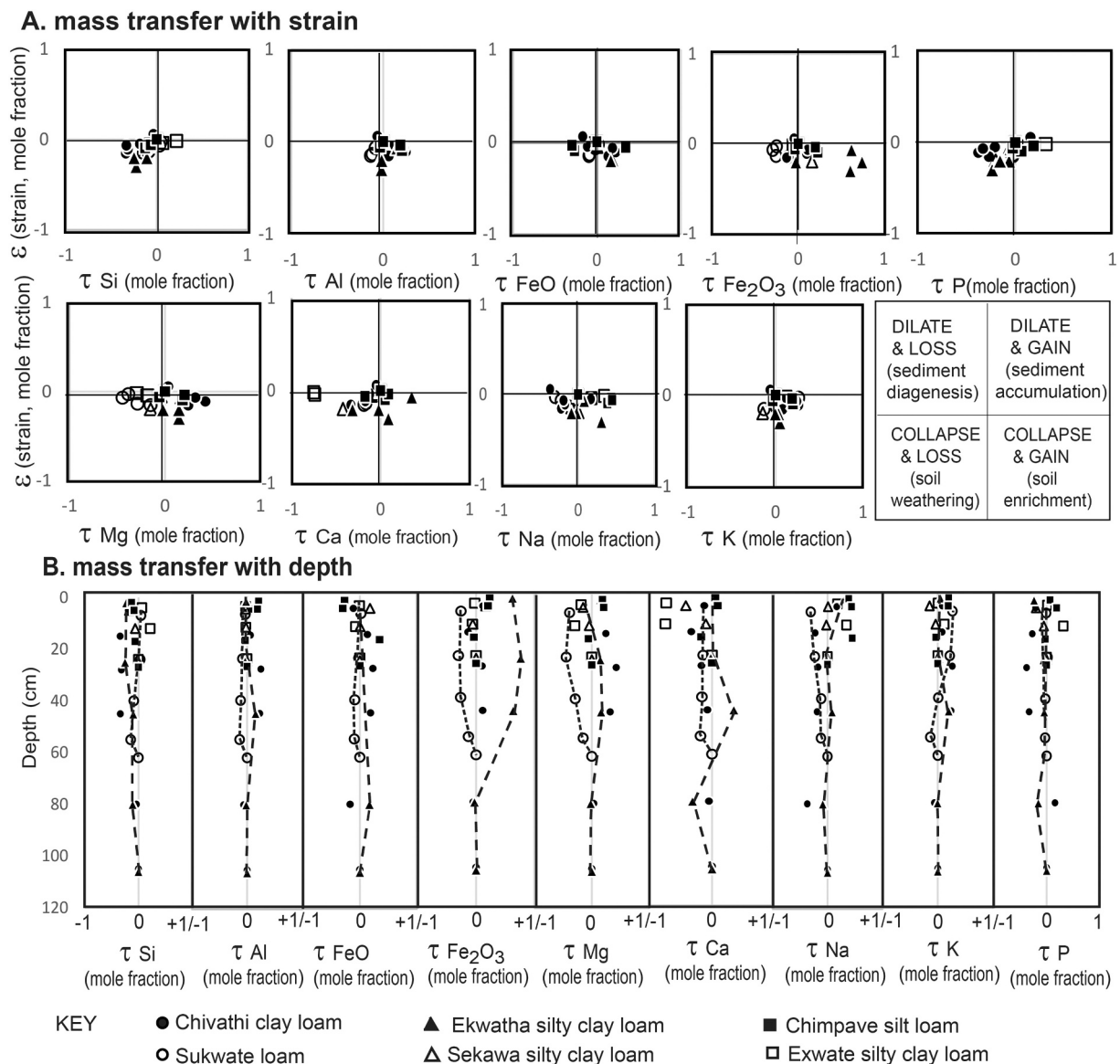
Fig. 8. Tau analysis of paleosols from the Chuar Group, including elemental mass transfer versus strain (A), and versus depth in paleosol profiles (B).

Cambrian, Ediacaran and Tonian paleosols, because they predate the evolution of stomates (Fig. 9). The $\delta^{13}C$ and $\delta^{18}O$ covariance may also be due to kinetic evaporative effects in narrow spaces of soils (Ufnar et al., 2008) or dry playa lakes (Talbot (1990), as further evidence of well drained soils. A photosynthetic production of organic carbon in the Chuar Group is clear from their organic carbon isotopic composition (Fig. 5G), biomarkers such as 25–28-bisnorgammacerane (Fig. 5K) and pristine/phytane ratios (van Maldegem et al. 2019). The isotopic covariance is neither destroyed nor enhanced by metamorphism to greenschist facies in paleosols of the Ordovician Juniata and Silurian Bloomsburg Formations (Fig. 9A), which have carbonate much more altered by burial recrystallization than paleosols of the Chuar Group.

6. Paleosol interpretation

6.1. Paleosol identification

The preceding paragraphs outline a variety of paleosol features in selected red and purple horizons of the Chuar Group, but the rest of this paper explores the kinds of paleosols present and their paleoenvironmental implications. The 66 beds regarded as paleosols (Fig. 5) have

been given non-genetic names (Tables 6-7) using the Havasupai language (Sinyella and Crawford 1984). These pedotypes can be interpreted in terms of soil taxonomy and various soil-forming factors to build detailed models of their paleoenvironment (Fig. 11). Paleosols in the Chuar Group form two distinct associations, a non-calcareous purple (5R) association with hematite and high organic content (Chimpave, Chivathi, Exwatha pedotypes) and a calcareous red (10R) association with hematite and low organic content (Sukwate, Sewaka, Ekwate, Keechika, Ematsile, and Kaveke pedotypes). Many of these are weakly developed with relict bedding, but of the purple group, the Exwatha pedotype has large gypsum sand crystals (Fig. 6C) which take millennia to form in modern soils (Retallack 2019), and so represented large areas of stable landforms. Of the red group, the best developed is the Sukwate pedotype with subsurface calcite nodules (Fig. 6D).

These pedotypes can also be identified within soil classifications (Stace et al. 1968; Isbell 1996; Soil Survey Staff 2014). In the FAO map classification (Food and Agriculture Organization, 1977) the purple noncalcareous gypsiferous Exwatha pedotype was Gleyic Solonchak, and would represent a map code of Zg + Jt,Jd (Table 7). The closest modern match is map unit Zg1-3a + Jt, Gp in humid, semihot, equatorial, mangrove swamps of the Orinoco Delta of Delta Amacuro State,
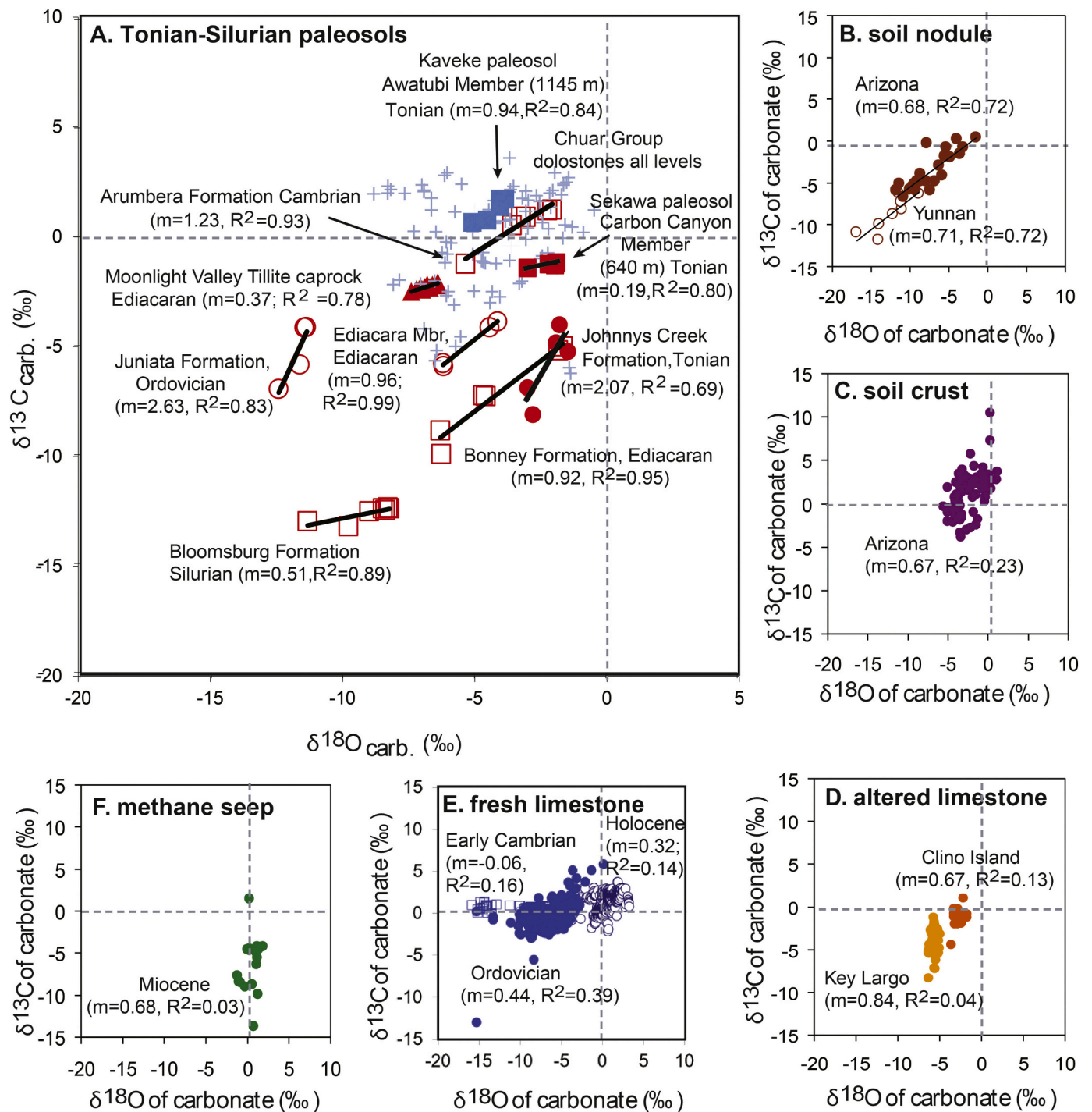
Fig. 9. Covariation of carbon and oxygen isotopic composition of carbonate as a characteristic of paleosols of the Chuar Group (Sewaka and Kaveke profiles), as opposed to no correlation in marine carbonate of the Chuar Group (crosses): (A), Chuar Group marine and estuarine dolostones (crosses), pedogenic carbonate (Sewaka at 640 m) in the Carboin Canyon Member and a meteorically weathered dolostone (Kaveke at 1145 m) in the Awatubi Member (Dehler et al. 2005, 2017), Tonian Johnnys Creek Formation in Ellery Creek, central Australia (Retallack, unpublished data), early Ediacaran cap carbonate of Moonlight Valley Tillite at Moonlight Valley, Western Australia (Bao et al. 2012), Ediacaran paleosols of South Australia (Retallack et al. 2014), Cambrian Arumbera Formation at Ross River (Retallack unpublished data), Ordovician paleosols of Pennsylvania (Retallack 2015b), and Silurian paleosols of Pennsylvania (Retallack 2015a); B, soil nodules (above Woodhouse lava flow, near Flagstaff, Arizona (Knauth et al. 2003) and in Yuanmou Basin, Yunnan, China (Huang et al. 2005); C, soil crusts on basalt (Sentinel Volcanic Field, Arizona, from Knauth et al. 2003); D, Quaternary marine limestone altered diagenetically by meteoric water (Key Largo, Florida, Lohmann 1988, and Clino Island, Bahamas, Melim et al. 2004); E, Holocene (open circles) and Ordovician (open squares) unweathered marine limestones (Veizer et al. 1999) and Early Cambrian (closed circles), Ajax Limestone, South Australia (Surge et al. 1997); F, marine methane cold seep carbonate (Miocene, Santa Cruz Formation, Santa Cruz, California (Aiello et al. 2001). Slope of linear regression (m) and coefficients of determination (r²) show that carbon and oxygen isotopic composition is significantly correlated in soils and paleosols, but not in other settings.

Table 6

Pedotypes and diagnosis for the Chuar Group, Arizona.

Pedotype	Mean-ing	Diagnosis	USDA (Soil Survey Staff 2014)	FAO (1977, 1978)	CLASSIC (Stace et al. 1968)	AUSTRAL-IAN (Isbell 1996)
Chimpave	kidney	Purple (5R)-green mottled claystone (A) over purple hackly claystone (Bw).	Fluvent	Dystric Fluvisol	Alluvial soil	Stratic Rudosol
Chivathi	liver	Purple(5R)-green mottled claystone (A) over nodular pyrite (Bg) and shale (C)	Sulfaquent	Thionic Fluvisol	Humic Gley	Sulfidic Rudosol
Ematsile	sand	Cracked and deformed red (10R) sandstone (A) over bedded orange sandstone (C)	Psamment	Dystric Regosol	Siliceous sand	Arenic Rudosol
Exwate	red	Red (10R) claystone (A) over hackly red claystone (Bw)	Ochrept	Calcic Cambisol	Brown clay	Brown Orthic Tenosol
Ekwatha	yellow	Purple (5R) claystone (A) over gray to purple claystone with gypsum nodules (By)	Gypsid	Gleyic Solonchak	Brown clay	Gypsic Hydrosol
Kaveke	split	Cracked gray dolomite (A) over pyritic dolomite (By)	Orthent	Lithosol	Calcareous sand	Leptic Tenosol
Keechika	little	Red (10R) hackly claystone (A) over brown bedded siltstone (C)	Fluvent	Eutric Fluvisol	Alluvial soil	Stratic Rudosol
Sekawa	egg	Red (10R)-green mottled claystone (A) over red siltstone with calcareous nodules (Bk).	Calcid	Calcic Yermosol	Red-brown earth	Calcenic Tenosol
Sukwate	green	Green claystone (A) over red (10R) claystone (Bw) and calcareous nodules (Bk)	Calcid	Calcic Xerosol	Calcareous red earth	Calcic Calcarosol

Note: Indigenous names for pedotypes are from Havasupai language (Sinyella and Crawford 1984).

Table 7

Interpretation of pedotypes for the Chuar Group, Arizona.

Pedotype	Paleoclimate	Ecosystems	Parent materials	Palaeotop-ography	Time for formation (yrs)
Chimpave	Not diagnostic	Early successional microbial mats	Quartzo-feldspathic silt	Intertidal flat	100
Chivathi	Not diagnostic	Intertidal microbial earth	Quartzo-feldspathic silt	Intertidal flat	10,000
Ematsile	Not diagnostic	Early successional microbial earth	Quartzo-feldspathic silt	Fluvial levee	100
Ekwatha	Hyperarid (132 ± 129 mm mean annual precipitation), temperate (11.9 ± 0.5 °C mean annual temperature)	Intertidal microbial earth	Quartzo-feldspathic silt	Coastal salina	11,800 ± 15,000
Exwate	Not diagnostic	Mid-successional microbial earth	Quartzo-feldspathic silt	Fluvial levee	1000
Kaveke	Not diagnostic	Endolithic microbial crust	Lithified dolostone	Beachrock exposure	100
Keechika	Not diagnostic	Early successional microbial earth	Quartzo-feldspathic silt	Streamside swale	100
Sekawa	Arid (284 ± 147 mm mean annual precipitation), seasonal (46 ± 22 mm mean annual range of precipitation), temperate (9.4 ± 0.5 °C mean annual temperature)	Microbial earth	Quartzo-feldspathic silt	Well-drained coastal terrace	33,000 ± 1800
Sukwate	Semiarid (386–459 ± 147 mm mean annual precipitation), (28–38 ± 22 mm mean annual range of precipitation) and temperate (8.9 ± 0.5 °C mean annual temperature)	Microbial earth	Quartzo-feldspathic silt	Well drained coastal terrace	8800–15,400 ± 1800

Venezuela (Food and Agriculture Organization 1971). At nearby Tucu-pita, mean annual temperature is 26.3° C, mean annual precipitation is 1397 mm, and mean annual range of precipitation 238 mm (Merkel 2020). Thionic Fluvisols (map code Jt) are found in intertidal mangroves throughout the tropics (Retallack 2013), but are uncommon in Central and North America (Food and Agriculture Organization 1975a, 1975b). The red calcareous Sukwate pedotype has subsurface micritic nodules like Calcic Xerosols, in a red association of Xk + Bk, Yk, Je, Rd, most like map unit Xk2-2a + Yk under Caribbean thorny woodland and cactus shrubland on the coastal plan between Punta Gallinas and Riohacha, Colombia (Food and Agriculture Organization 1971). At nearby Rio-hacha, mean annual temperature is 28.3° C, mean annual precipitation is 588 mm, and mean annual range of precipitation 175 mm (Merkel 2020).

6.2. Original parent material

Parent materials to paleosols of the Chuar Group were largely quartzo-feldspathic silt and kaolinite-illite clay (Fig. 7; Dehler et al. 2005). Feldspars include limpid and tartan-twinned K-feldspar from granitic rocks, as well as twinned plagioclase laths from airfall volcanic tuffs (Dehler et al. 2017). Abundant silt-sized quartz and feldspar may

also be eolian loess, which is common in both non-marine and marine rocks older than Cambrian and predating substantial vegetation cover of the land (Dalrymple et al. 1985; Retallack 2011b, 2013). Loess plains are a likely parent material for the calcareous red paleosols (Sukwate, Sewaka, Ekwate, and Keechika pedotypes). These paleosols are domi-nantly illitic (Dehler et al. 2005), probably from diagenetic alteration of smectite (Novoselov and de Sousa Filho, 2015) giving modest potash enrichment (Fig. 8). Red paleosols of the Carbon Butte and Carbon Canyon Members have detrital zircons mostly from Paleoproterozoic rocks (1600–1800 Ma: Dehler et al. 2017). Loess is today among the most productive of modern soil parent materials, rich in weatherable minerals and physically stable for cultivation (Swineford and Frye 1951; Fehrenbacher et al. 1986).

In contrast the non-calcareous, kaolinitic purple paleosols (Chim-pave) have high amounts (0.57–3.51 wt% C) of organic matter, and some have abundant pyrite and marcasite (Chivathi) like intertidal soils that today support tropical mangroves (Retallack 2013). Kaolinite in the purple paleosols (Fig. 5) would have been derived from well drained, upland, humid, soils (Dehler et al. 2017).

6.3. Reconstructed sedimentary setting

Detrital zircon age spectra of the Chuar Group (Dehler et al. 2017) are evidence of source terranes in Mesoproterozoic and Paleoproterozoic rocks to the west (Figs, 2, 10). Loess is suggested by abundant silt-sized grains (Fig. 7). Freely drained, red, silty paleosols (Sukwate, Sewaka, Ekwate, and Keechika pedotypes) have the petrographic appearance of loess in the lowest part of their profiles. Loess plains now form distinctive landforms often called "rolling downs", but with steep angle of repose of terraces and erosional gullies near streams, because of their angular silt grains (Zakrewska, 1963). Other red sandy paleosols (Ematsile) with limited destruction of parting lamination (Fig. 4H) were probably fluvial levee soils, because they overlie trough cross bedded sandstone of the lower Carbon Butte Member interpreted as paleochannels (Fig. 5).

In contrast, purple paleosols with pyrite and marcasite (Chivathi) retain fine lamination like soils of intertidal mudflats (Retallack 2013). Intertidal paleosols under salt marsh and mangal are widely distributed in soil maps (Soil Survey Staff 1971, 1975a, 1975), but comparable Tonian soils would have supported only microbes and microbial consortia (Retallack 2012a). Other purple paleosols (Chimpave) are associated with stromatolitic dolostones, which show local ferruginization and cracking as evidence of subaerial exposure within the intertidal and supratidal zone (Dehler et al. 2001, 2005). Another kind of purple paleosol (Ekwatha) has gypsum sand crystals characteristic of well drained, desert soils (Watson 1985; Al Kofahi et al., 1993) and unlike limpid crystals of gypsum and anhydrite in marginal marine or lacustrine sabkhas (Renaut and Tiercelin, 1994; Ziegenbalg et al. 2010). Ekwatha paleosols were locally well drained, but closely associated with stromatolites and intertidal soils, so may have been coastal salinas of low coastal terraces (Fig. 10A), like Salina Sauca, Venezuela (Mendez and Carthaya, 2001) and Garden Point, Shark Bay, Western Australia (Cockbain 1976; Collins and Jahnert 2014).

6.4. Time for formation

The duration of soil formation, derived from chronofunctions of modern soils, give insights into breaks in sedimentation and sediment accumulation rates of sequences of paleosols. Duration of soil formation for type Sukwate and Ekwatha pedotypes (Fig. 7) can be calculated from chronofunctions for the rate of formation of nodules and desert roses in modern soils of low productivity. These are at best only rough estimates for Precambrian soils of unknown productivity. Diameter of pedogenic-carbonate nodules (D in cm) is related to radiocarbon age of nodules (A in kyrs) near Las Cruces, New Mexico ($r^2 = 0.57$, s.e. = $\pm$ 1.8 kyr, $p = 0.001$), as follows (Retallack 2019).

$$A = 3.92D^{0.34} \text{ eq. (5).}$$

Similarly, abundance of gypsum in a profile (G as % surface area using comparison chart of Terry and Chilingar 1955) is a metric for age (A in kyrs) in the Negev Desert of Israel ($r^2 = 0.95$, s.e. = $\pm$15, and $p < 0.01$), as follows (Retallack 2019). Standard errors in both eqs. 5 and 6 are based on their modern soil training sets.

$$A = 3.987G + 5.774 \text{ eq. (6).}$$

The calcic chronofunction applied to Sukwate and Sewaka paleosols in the Carbon Canyon Member at 630 m is 13.7 ± 1.8 kyr and 3.3 ± 1.8 kyr, and for two Sukwate paleosols in the Carbon Butte Member at 1065 m is 15.4 ± 1.8 kyr and 8.8 ± 1.8 kyr. The gypsic chronofunction applied to an Ekwatha paleosol in the Tanner Member at 165 m had a duration of 11.8 ± 15 kyr. These Tonian paleosols are thus moderately developed, in the usual scale in which Holocene (up to 10 kyr) soils are moderately developed (Retallack 2019). Failure to recognize Precambrian paleosols within sedimentary successions is not due to their weak development. Destruction of relict bedding and formation of blocky pedal structure in paleosols of the Chuar Group can be very impressive (Fig. 4D-E).

Ekwatha paleosols with large pyrite nodules are comparable with similar post-Flandrian (ca.10 ka) intertidal paleosols today (Retallack 2013). Intertidal soils may be an unfamiliar concept for sedimentology of tidal facies, but are widely represented on soil maps under salt marsh and mangal vegetation (Soil Survey Staff 1975a, 1975b, 1977). Other paleosols are much less developed, a few millennia for Exwate, and a century or less for Chimpave, Ematsile and Keechika profiles with much relict bedding. These are maximal estimates, because based on comparison with homogenization of bedding in Pleistocene soils of the San Joaquin Valley, California (Harden 1982), which were more actively rooted and burrowed than likely for Tonian soils.

6.5. Paleoclimate

Gypsic and calcic horizons are today found at depths in soils proportional to mean annual precipitation (Retallack 2019), and this in turn
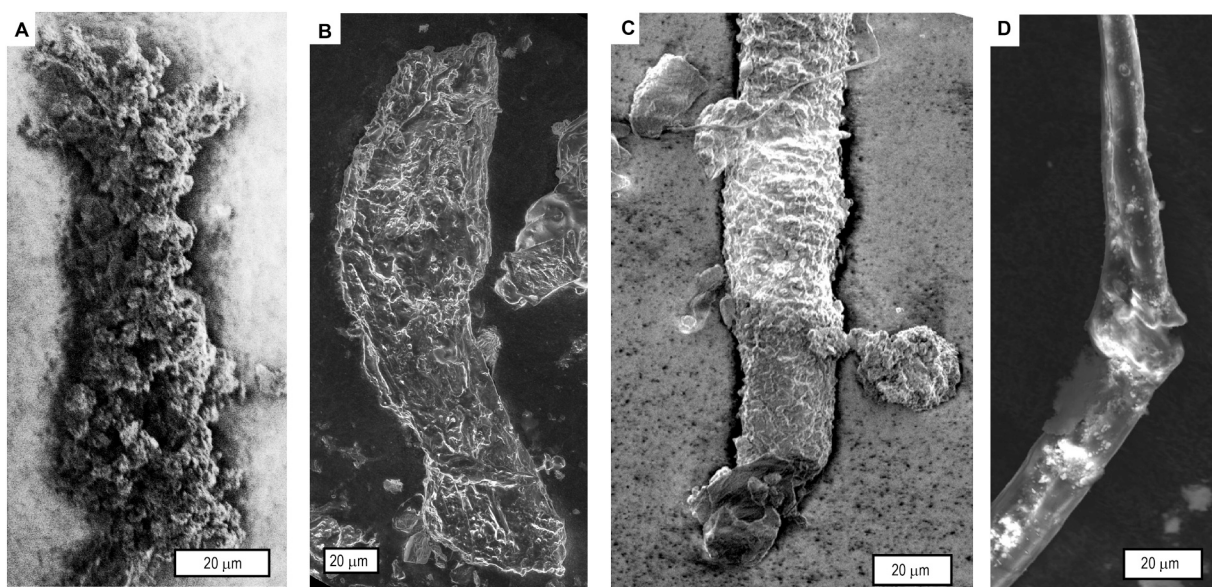

Fig. 10. Microfossils macerated from the Sekawa silty clay loam paleosol (A-B,D) and Sukwate loam paleosol (C): A, thread forming cyanobacteria, *Prasinema gracile*; B-D, fungal threads *Tortotubus protuberans*. SEM stubs in Condon Collection of Museum of Natural and Cultural History are F127276 (A), F127278 (B), F127283 (C) and F127281 (D).
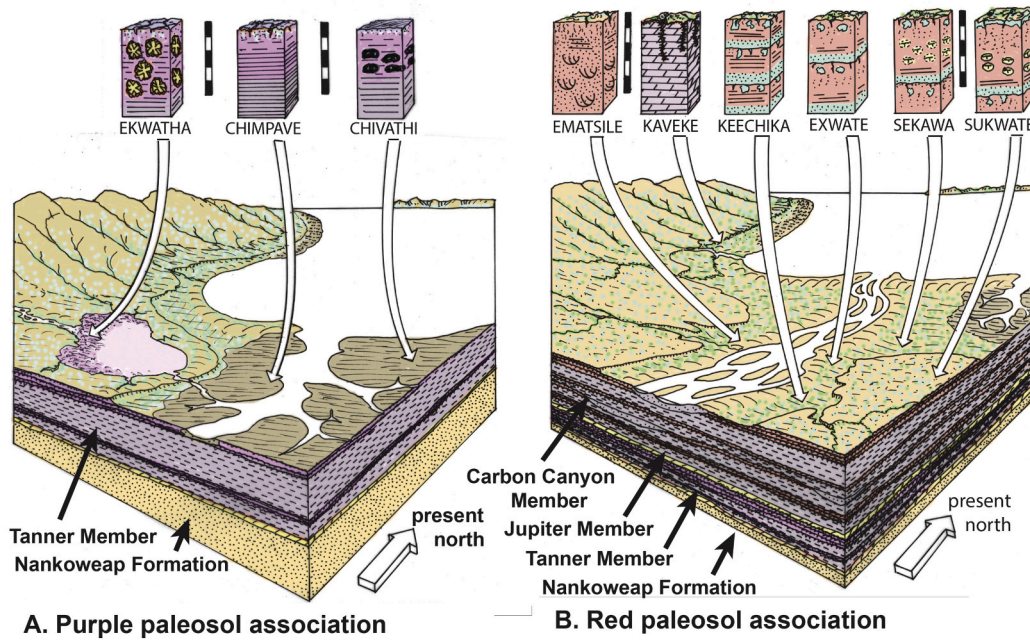
Fig. 11. Reconstructed Tonian soils of the Chuar Group, Arizona: A, purple (5R) paleosol association of the Tanner Member; B, red (10R) paleosol association of the Carbon Canyon Member. (For interpretation of the references to color in this figure legend, the reader is referred to the web version of this article.)
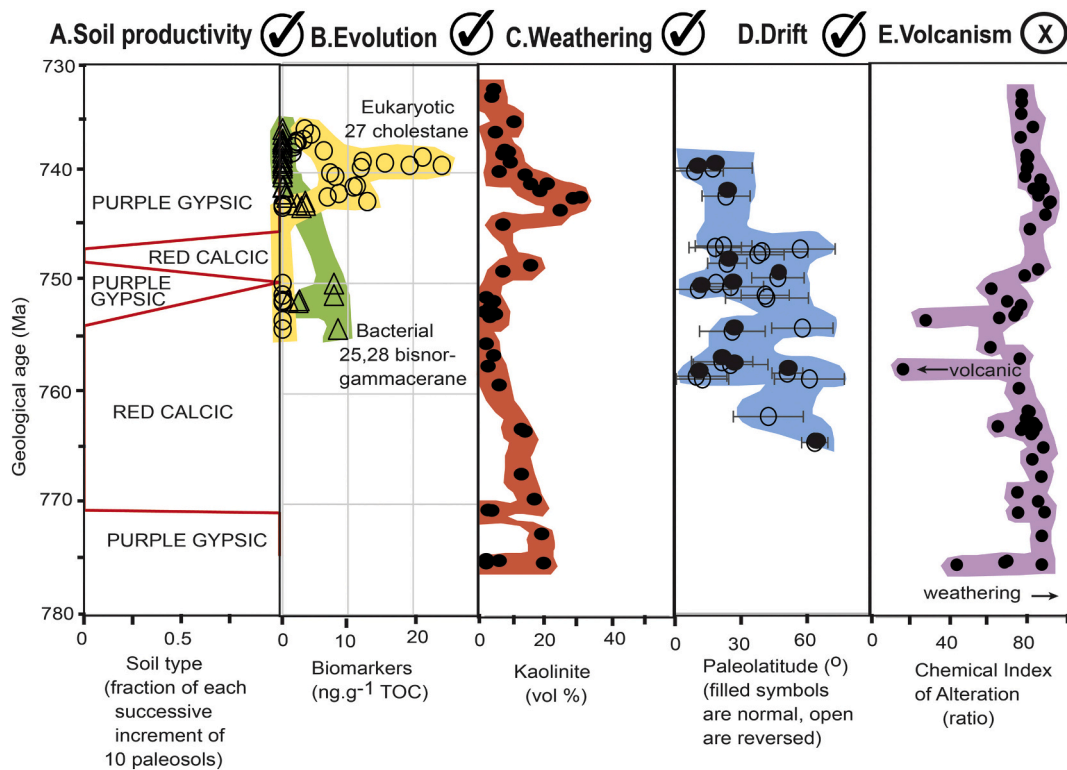

Fig. 12. Key Chuar Group time series for understanding the inception of Snowball Earth all plotted to the age model of eq. 1; A, Proportion of productive red calcic and less productive purple gypsic paleosols; B, decline on bacterial 25,28 bisnorgammacerene and rise in eukaryotic 27 cholestane (from van Meldegem et al., 2019); C, percent kaolinite in mudrocks (from Dehler et al. 2005); D, paleolatitudes (from Weil et al. 2004); and volcanic transients from Chemical Index of Alteration (Dehler et al. 2005). (For interpretation of the references to color in this figure legend, the reader is referred to the web version of this article.)

is related to soil productivity, which would have had a different relationship to precipitation during the Precambrian (Breecker and Retallack 2014). Calcic soils are widespread in aridlands, but gypsic soils form in extreme deserts such as the Atacama Desert of Chile (Navarro-

González et al. 2003; Ewing et al. 2008). For calcic paleosols, mean annual precipitation (P in mm) is related to depth in the profile to calcareous nodules (D in cm corrected for burial compaction by eq. 2) from a global compilation ($r^2 = 0.52$, s.e. $= \pm147$, and $p < 0.0001$), as

follows (Retallack 2019).

$P = 137.24 + 6.45D - 0.0132D^2$ eq. (7).

For gypsic soils, another global compilation gives mean annual precipitation from depth to gypsum (D again compaction corrected: $r^2 = 0.63$, s.e. $= \pm 129$, and $p < 0.00001$), as follows (Retallack 2019).

$P = 87.593e^{0.0209D}$ eq. (8).

Seasonality of precipitation, defined as wettest minus driest month mean precipitation (R in mm) is a function of thickness of the calcic horizon (T in cm), again from a global compilation with good precision ($r^2 = 0.58$, s.e. $= \pm 22$, and $p < 0.00001$) as follows (Retallack 2019).

$R = 0.79T + 13.7$ eq. (9).

The calcic climofunction applied to a Sukwate and Sewaka paleosol in the Carbon Canyon Member at 630 m is 459 ± 147 mm and 284 ± 147 mm, and for two Sukwate paleosols the Carbon Butte Member at 1065 m is 400 ± 147 mm and 386 ± 147 mm mean annual precipitation. The gypsic climofunction applied to an Ekwatha paleosol in the Tanner Member at 165 m had an estimated 132 ± 129 mm mean annual precipitation. These Tonian paleosols were thus hyperarid in the Tanner Member comparable to Aridisols in modern Atacama Desert, Chile (Ewing et al. 2006, 2008). During deposition of the Carbon Canyon Member climate was arid to semiarid with calcic paleosols like higher rainfall slopes surrounding Atacama lowlands (Navarro-González et al. 2003). Such arid climates are not at variance with coastal plain or intertidal sedimentary settings, as can be seen in modern coastal Peru and Baja California (Food and Agriculture Organization 1975a, 1975b, 1977).

Seasonality of precipitation, or wettest month average minus driest month average for a Sukwate and Sewaka paleosol in the Carbon Canyon Member at 630 m is 38 ± 22 mm and 46 ± 22 mm, and for two Sukwate paleosols the Carbon Butte Member at 1065 m is 35 ± 22 mm and 28 ± 22 mm mean annual range of precipitation. These are modest, non-monsoonal seasonalities (Retallack 2019).

Pedogenic paleothermometers based on soils of modern woody vegetation (Sheldon et al. 2002; Gallagher and Sheldon 2013) are not applicable to likely microbial earths of Precambrian paleosols (Retallack 2012a). A paleothermometer based on modern soils under lichen-shrub tundra vegetation of Iceland (Óskarsson et al. 2012) is the best option, predicting temperature (T in °C) from chemical index of weathering (CIW) (W in mole fractions) of non-calcareous Bw and By horizons, with good precision ($r^2 = 0.81$, s.e. $= 0.5$, $p < 0.001$). The CIW is similar to the better known Chemical Index of Alteration (CIA), in which CaO is non-carbonate, and values of 75–85% are temperate (Nesbitt and Young 1982).

$T = 0.21CIW - 8.93$ eq. (10).

$CIW = \frac{100Al_2O_3}{(Al_2O_3+CaO+Na_2O)}$ eq. (11).

$CIA = \frac{100Al_2O_3}{(Al_2O_3+CaO+Na_2O+K_2O)}$ eq. (12).

This CIW chemical proxy gives mean annual temperatures of 8.9 ± 0.5 °C and 9.4 ± 0.5 °C for a Sukwate and Sewaka paleosol in the Carbon Canyon Member at 1145 m, and 11.9 ± 0.5 °C for an Ekwatha paleosol in the Tanner Member at 165 m. These are all cold temperate climates, compatible with loess deposition and the coeval (752.1 Ma) Konnarock Glaciation of Virginia, USA (MacLennan et al. 2020). Cool paleo-temperatures are also compatible with mid-latitudes (59-25º) indicated by paleomagnetic data of the Carbon Canyon Member (Fig. 2B). Paleolatitudes were calculated using formulae of Haile (1975) and Butler (1992) from data of Weil et al. (2004), and declined from temperate to tropical by the level of the Walcott Member (Fig. 2B). Some support for declining paleolatitude and rising paleotemperature with Chuar Group deposition comes from a spike in kaolinite clay in the Awatubi Member (Fig. 5I), but chemical index of alteration did not change appreciably from temperate throughout the Chuar Group (Fig. 5J). Chemical Index of Alteration is a general weathering index usable for both paleosols and sedimentary rocks, but kaolinite proportions and paleomagnetic studies are more easily measured in red bed paleosols than in marine sediments. These indications of warmer climate than the CIW proxy, are

compromised by acid sulfate weathering as demonstrated for Ekwatha paleosols.

6.6. Life on land

Maceration of Sekawa and Sukwate paleosols in HF to remove clay has revealed a variety of soil microfossils (Fig. 10). Clayey soil agglutinated around central threads (Fig. 10A) is similar to the problematic fossil *Prasinema gracile* (Retallack 2011b), considered remnants of rope-forming cyanobacteria (Garcia-Pichel and Wojciechowski 2009). Other elongate fossils (Fig. 10B-D) are similar to the problematic fossil *Tortotubus protuberans* (Johnson 1985), including multiple hyphae within a papillate envelope (Fig. 10B), lateral branches (Fig. 10C), and paired hyphae (Fig. 10D). *Tortotubus* has been interpreted as a dikaryan (Ascomycota+Basidomyctoa) fungal cord by Smith (2016), but lacks definitive dikaryan freatures, and these hyphae and other Mesoproterozoic fossils could as easily be Mucoromycotina or Glomeromycota known from palynomorphs of Mesoproterozoic age (Retallack 2015c; Loron et al. 2019).

Thin sections show lack of lamination in paleosol surface horizons, due in part to observed cracking (Fig. 6A-B). Also observed are green haloed threads in claystone (Fig. 4D) like the ichnofossil *Prasinema gracile* interpreted as thread-forming soil microbes (Retallack 2011b). That interpretation has been disputed based on false assumption that they were loose specimens (Jago et al. 2012), but both those Australian (Retallack 2012b), and these Arizona drab threads are in place within red paleosols (Fig. 4D).

The Chuar paleosols also show 20–31% surficial depletion of phosphorus (Fig. 8), another indication of a microbial earth soil community consuming this essential micronutrient (Neaman et al. 2005a, 2005b). Marine sediments, in contrast, show little change in phosphate with depth or substantial enrichment in phosphate (Filippelli, 2011).

Another indication of paleosol productivity is the amount of soil-respired CO_2 inferred from relationships with depth to gypsic and calcic horizons in modern soils, corrected for burial compaction (using eq. 3) for application to paleosols. The transfer functions for soil-respired CO_2 from Breecker and Retallack (2014) are eq. 11 for gypsic horizons ($r^2 = 0.64$; S.E. ± 552; $p < 0.05$), and eq. 12 for calcic horizons ($r^2 = 0.66$, S.E. ± 768 ppmv, $p < 0.0001$). This secondary productivity of CO_2 controls the level at which soluble salts can be precipitated in the soil, and is also related to mean annual precipitation, which also controls terrestrial productivity (eqs. 7–8).

$P_r = 42.9D_g + 399$ eq. (11).

$P_r = 35.3D_s + 588$ eq. (12).

The calcic transfer function applied to a Sukwate and Sewaka paleosol in the Carbon Canyon Member at 630 m is 2573 ± 768 ppm and 1430 ± 768 ppm, and for two Sukwate paleosols the Carbon Butte Member at 1065 m is 2172 ± 768 ppm and 1820 ± 758 ppm. In contrast, the gypsic transfer function applied to an Ekwatha paleosol in the Tanner Member at 165 m had only 1239 ± 552 ppm soil CO_2. Thus soil productivity increased during deposition of the Chuar Group.

Increased productivity through time is also apparent in the transition from gypsic (Ekwatha) paleosols near the base of the section to mainly calcic (Sukwate, Sekawa) paleosols in the Carbon Butte Member, but it was reversed by marine transgression and gypsic paleosols in the Awatubi and Walcott Members (Fig. 5). Comparable community transitions and their microbiome have been studied in the Atacama Desert of Chile, where gypsic soils of the hyperarid valley bottom playas pass upward to calcic soils of semiarid slopes (Rech et al. 2003; Quade et al. 2007). Hyperarid gypsic soils have low overall diversity of cyanobacteria and actinobacteria, but semiarid calcic soils have greater diversity of fungi, archaea, algae, bunch grass and saltbush (Quade et al. 2007; Castillo and Beck 2012; Neilson et al. 2012, 2017; Vitek et al., 2013; Araya et al. 2020). Much of the biota of hyperarid gypsic soils is dormant, and revives only after rare rains (Crits-Cristoph et al., 2013). Lichens aid formation of carbonate in calcic soils from excretion of precursor oxalate

(Verrechia et al., 1993; Giordani et al. 2003; Vitek et al., 2013). Another modern analog for transition from cyanobacterial to lichen communities is ecological succession in western North American desert soil crusts, which show the following stages: 1, bare soil; 2, large filamentous cyanobacteria such as *Microcoleus vaginatus*; 3, gelatinous lichens such as *Collema coccophorum*; 4, squamulose lichens such as P*sora cerebriformis*; 5, crustose lichens such as *Diploschistes scruposus*; 6, liverworts such as *Cephaloziella divaricata*; 7, short mosses such as *Bryum argenteum*; 8, foliose lichens such as *Xanthoparmelia convoluta*; 9, tall mosses such as *Syntrichia ruralis*; 10, fruticose lichens such as *Aspicilia filiformis*; 11, early successional angiosperms such as *Chrysothamnus nauseus*, and 12, late successional angiosperms such as *Artemisia tridentata* (Rosentreter 1984; Belnap et al. 2001). The gypsic-calcic transition in the Chuar Group may reflect evolution to successional stage 6 by the deposition of the Awatubi Formation, with land plants evolving perhaps by Cambrian (Strother et al. 2017).

From this perspective, a variety of other fossils and biomarkers from the Chuar Group assumed to have been marine (Schopf et al. 1973; Bloeser 1985; Porter and Knoll 2000; Porter et al. 2003; Dehler et al. 2005; van Maldegem et al. 2019), may need to be reconsidered, reviving former interpretations of the Chuar Group as terrestrial (Ford and Breed 1973), or lacustrine (Reynolds and Elston 1986; Reynolds et al. 1988; Cook 1991). The most common coccoids, hyphae (Schopf et al. 1973), acritarchs (Vidal and Knoll 1983; Horodyski and Bloeser 1983; Vidal and Ford 1985), *Chuaria* carbonaceous discoids (Ford and Breed 1977), and testate amoebae (thecamoebans) such as *Melanocyrillium* were found within black and gray shales and cherts that are interpreted here as aquatic, and probably marine (Table 1). Fossils in lacustrine and shallow marine lagoons are often overwhelmingly terrestrial leaves, pollen, and other plant debris (Pappazoni et al., 2014; Barreda et al. 2020), and other Tonian lakes and shallow marine shales have been found with a mix of aquatic and terrestrial microfossils (Strother et al. 2011). Microfossils in silicified pisolites of the lower Awatubi Member have been interpreted as prokaryotic cyanobacteria, eukaryotic green algae, and fungi (Schopf et al. 1973; Horodyski and Bloeser 1983).

Eomycetopsis from the Chuar Group was initially interpreted as fungal hyphae (Schopf et al. 1973), but was later considered cyanobacterial sheaths because they lacked septae and reproductive structures (Knoll and Golubic 1992). The copious branching and aseptate condition of *Eomycetopsis* is similiar to glomeromycotan fungi, now known from fossil spores well back into the Proterozoic (Retallack 2015c; Loron et al. 2019). *Chuaria* was most likely a cyanobacterial ball (Ford and Breed 1977; Hofmann 1977), or perhaps a green alga (Kumar 2001) or microbial colony (Grazhdankin and Gerdes 2007; Grazhdankin et al. 2012).

Living relatives of thecamoebians are now soil protists, and it is possible that the known fossils were washed out to sea (Bloeser 1985; Porter and Knoll 2000; Porter et al. 2003). Tonian thecamoebians from intertidal heterolithic facies of Red Pine Creek in the Uinta Mountains (Fig. 2A) were in freshwater determined by boron assay, but other assays in the same study show that the Tonian alga *Tenuocharta cloudii* from Horsethief Springs, California (Fig. 2A) was fully marine (Retallack 2020).

Stromatolites in the Chuar Group include *Baicalia, Inzeria, Stratifera,* and *Boxonia*, comparable with assumed marine stromatolites around the world (Walter 1972, 1976). However, stromatolites are both marine and freshwater now (Cockbain 1976; Wacey et al. 2018), and in the past (Corkeron et al. 2012; Coffey et al. 2013). Ferruginized paleokarsts on stromatolitic limestones, such as the polygonal marker bed of Dehler et al. (2001, Fig. 3E), are evidence of prolonged exposure of some of these stromatolitic dolostones.

Biomarkers were mostly extracted from gray to black organic-rich shales of the Chuar Group here interpreted as marine to lacustrine (Table 1), rather than oxidized paleosols. A general decline pristine/phytane ratios, 25–28-bisnorgammaracene, and alkane-kerogen $\delta^{13}C$, but increasing C^{27} cholestane up section, have been interpreted as a

decline in cyanobacteria, but rise in algae or fungi within the upper Awatubi Member (van Maldegem et al. 2019; Zumberge et al., 2020). C^{27} cholestane is found widely in fungi, red algae, and animals (Weete et al. 2010; Brocks et al. 2017), and it rises in the Awatubi Member, reaches a peak in the lower Walcott Member, then declines abruptly in the upper Walcott Member, which is largely marine-lagoonal black shale (Fig. 5K). This eukaryotic biomarker may thus have been in part terrestrial.

7. Conclusions

7.1. What caused Snowball Earth?

Evidence collected here to address the cause of Snowball Earth some 12 m.yr after the deposition of the Chuar Group is assembled against the age model (eq. 1) in Fig. 12, in order to address four conflicting hypotheses of (1) evolutionary advances in life on land (Hedges 2003); (2) evolutionary advances in marine life (Tziperman et al. 2011), (3) continental drift into intensely weathered, warm-humid, tropical regions of Siberian, southern African and Australian cratons (Hoffman and Schrag 2002; Hoffman and Li 2009), and (4) large amounts of easily weatherable materials or aerosols produced by volcanism (Donnadieu et al. 2004; MacDonald and Wordsworth, 2017; Stern and Miller 2018; Long et al. 2019; Arnscheidt and Rothman 2020). Only the idea of volcanism stimulating weathering and carbon consumption in the Chuar Group is unlikely, because the chemical index of alteration is consistent, with only a few horizons of volcanic ash indicated by unusually low values (Fig. 12E). The idea of continental drift into low latitudes is supported by paleomagnetic data from the Chuar Group (Fig. 12D), and corresponds with an increase in weathering intensity from increased abundance of kaolinite, rather than illite and other clays (Fig. 12C). There are two odd things about this: (1) kaolinite abundance declines after spiking in the Awatubi Member (Fig. 12C), and (2) the lower paleolatitude and kaolinite spike had only a limited effect on overall weathering revealed by Chemical Index of Alteration (Fig. 12E). Paucity of paleosols in the upper Awatubi and Walcott Members (Fig. 5) is evidence that declining kaolinite and weathering at that level was due to marine transgression. Paleosols of the Carbon Butte, Duppa, Carbon Canyon, and Jupiter Members are a better guide to changing weathering on land.

In a biotic explanation for the onset of Snowball Earth, Tziperman et al. (2011) argue that increased complexity and biomass of marine organisms, principally eukaryotic algae, increased carbon burial in the ocean. The rise of algae is also considered causal by Feulner et al. (2015), who argue that atmospheric cooling to Snowball Earth was by algal emission of aerosolic dimethyl sulfide. These views are supported by black shale and biomarker abundance in the Chuar Group, particularly the decline of cyanobacterial 25–28-bisnorgammacerane and rise of eukaryotic C^{27} cholesterane (Fig. 12B). Other indirect lines of evidence for late Tonian evolution include a variety of trends in marine rocks: decreased aluminum phosphate in nearshore marine metaquartzites (Morteani et al. 2007), more complex clay polytypes in marine shales (Kennedy et al. 2006), onset of significant paleokarst diagenesis of carbonates (Knauth and Kennedy 2009), and higher strontium isotopic composition of marine limestones (Kennedy 2013).

These changes have been assumed to have been marine, but could they have been from increased terrestrial weathering delivering more nutrient cations into the ocean? A marine or post depositional origin of kaolinite by hydrothermal activity is possible (Marumo and Hattori 1999; Dekov et al. 2005), but unlikely in the absence of high temperature mineralization, and thermal immaturity of organic matter in the Chuar Group (van Maldegem et al. 2019; Zumberge et al., 2019). The rise in kaolinite corresponds to abundance of red paleosols of greater secondary productivity (2573–1430 ppm soil CO_2) than purple paleosols (only 1239 ± 552 ppm soil CO_2: Fig. 12A). If the modern gypsic-calcic ecosystem transition in the Atacama Desert is a guide, then low diversity cyanobacteria-actinobacteria communities were enriched by

fungi, archaea, algae, and protists (Quade et al. 2007; Castillo and Beck 2012; Neilson et al. 2012, 2017; Vitek et al., 2013; Araya et al. 2020). A plausible biological hypothesis for Cryogenian acceleration of silicate weathering is the evolution or geographic expansion of mycorrhizal fungi, megascopic lichens, or other microbial consortia on land (Hedges 2003). This would have been a substantial advance in weathering over Paleoproterozoic life on land of only discoidal microbial colonies and social amoebae (Hofmann et al. 1990; Grazhdanhkin et al., 2012), small endosymbiotic fungi (Retallack 2015c), and resistant, complexly layered spore walls of fungi comparable with living mycorrhizal Glomeromycota (Loron et al. 2019). Fungal hyphae and tissue fragments are known from Tonian, Cryogenian and Ediacaran rocks (Yuan et al. 2005; Agić et al. 2019; Bonneville et al. 2020). Weathering intensity under modern lichens is 2–18 times that of nearby abiotic rock surfaces (Brady et al. 1999). Weathering under calcic ecosystems is deeper and more intense than gypsic ecosystems and sequesters 6 times more soil organic carbon (Ewing et al. 2006, 2008).

Our working hypothesis is that Snowball Earth glaciations were triggered by evolution of megascopic terrestrial organisms, perhaps eukaryotic fungi and lichens, which deepened soils, increased respired soil-CO_2, promoted chemical weathering of base cations, enlarged terrestrial biomass, and ameliorated soil salinity to create the most productive terrestrial ecosystems known up to that time (Hedges 2003). Deeper terrestrial weathering also would have delivered higher fluxes of cationic nutrients, bicarbonate, and differences in isotopic composition to marine rocks (Morteani et al. 2007; Kennedy 2013; Knauth and Kennedy 2009). In the same way, Hirnantian glaciation may have been induced by Ordovician evolution of liverworts and mosses increasing the depth and degree of weathering on land (Lenton et al. 2012; Retallack 2015b). Permo-Carboniferous glaciation may have resulted from Devonian evolution of forests with clayey (Alfisol and Ultisol) and peaty (Histosol) soils (Berner 1997; Retallack 2019). Pleistocene glaciation may have been the result of Cenozoic evolution of grasslands with organic-rich (Mollisol), moist, high albedo soils (Retallack 2019). Compared with these other major evolutionary advances in biomass and soil carbon storage on land, fungi and lichens would have been more widespread on land because they are hardy in frigid alpine and polar environments. These differences may explain why Cryogenian glaciations extended to much lower latitudes than Ordovician, Permo-Carboniferous or Pleistocene glaciations (Hoffman and Li 2009; Retallack 2011a). Liverworts, trees and grasses are sensitive to freezing, and their latitudinal and altitudinal limits (Harsch and Bader 2011) are lower than for cyanobacteria, algae, fungi and lichens (Belknap et al., 2001). Liverworts, trees, and grasses were consecutive additions to terrestrial ecosystems (Retallack 2015a, 2015b, 2019), building on, but not completely displacing a framework of lichen weathering on land that may have been established as early as the Tonian (Hedges 2003). Our biotic explanation for Neoproterozoic Snowball Earth is compatible with data from the Chuar Group, and now needs testing in other sections.

7.2. Chemostratigraphic correlation by greenhouse crises or glacioeustatic regressions?

Correlation of isotopic or other chemical fluctuations in Precambrian rocks has become an important tool for local and international stratigraphic correlation (Dehler et al. 2017; Hay et al. 2019). Once obvious diagenetic artefacts are removed, the fluctuations are considered changes in global ocean chemistry (Dehler et al. 2005; Corkeron 2007, 2008; Halverson et al. 2010; Swanson-Hysell et al. 2012). This study has shown that this assumption may not be warranted for the Chuar Group which has at least 66 discrete paleosols as evidence of early diagenetic soil formation within 1622 m of section (Fig. 5), based on a variety of criteria including distinctive vertical cracking patterns, abundant eolian silt, replacive gypsum and calcite nodules, mineral distribution, within-bed strain and mass transfer, and stable isotopic covariance outlined above. Initial chemostratigraphy of the Chuar Group came from $\delta^{13}C$ of

organic matter and carbonate, which remained separated by a constant amount ($\delta^{13}C_{carb}$.- $\delta^{13}C_{org}$. = 28‰). While very negative $\delta^{13}C_{org}$ can be explained by anaerobic sulfur bacteria or methanogens (Schidlowski 2001), the same is not true for negative $\delta^{13}C_{carb}$. (Fig. 9), which is largely known from pedogenic carbonate (Retallack 2016b) or meteoritically altered limestone (Knauth and Kennedy 2009). As expected, paleosols were found at each very negative inflection of the $\delta^{13}C_{carb}$ curve at 30, 180, 640, 1000, 1270 and 1410 m (Fig. 5G), and several beds have the distinctive covariance of $\delta^{13}C_{carb}$. and $\delta^{18}O_{carb}$. found in pedogenic nodules and weathered limestone (Fig. 9). The most negative of these excursions was at about 1000 m, but poorly constrained because red beds below were undersampled. This negative excursion to paleosols is at 752 Ma in the age model (eq. 1), and corresponds with the 752 Ma Konnarock Glaciation of Virginia (MacLennan et al. 2020). Very negative inflections in supposed marine stable isotopic curves are also found in both the Sturt and Elatina glaciations of the Cryogenian (Retallack 2011a; Swanson-Hysell et al. 2012), and in the Gaskiers, Fauquier and Billy Springs glaciations of the Ediacaran (Retallack et al. 2014). These were not panoceanic inflections in isotopic composition (Giddings et al. 2010; Grotzinger et al. 2011), but times when sea level dropped due to glacial advances to allow formation of calcic paleosols and meteoric weathering of limestone paleocanyons (Retallack et al. 2014, 2015).

The unusually isotopically light $\delta^{13}C$ of carbonate inflection points used for chemostratigraphy has also been attributed to an oceanic crisis of methane degassing (Kennedy et al. 2008), but close examination of the locality which was the basis for that hypothesis (Retallack et al. 2015) failed to find a methanogenic signature as in Fig. 9. Other ideas are that voluminous marine volcanism was the source of alkalization (Gernon et al. 2016), or that a stagnant CO_2 reservoir in a stratified deep ocean was released castastrophically (Grotzinger et al. 2011). None of these mechanisms work for Chuar Group deposited at the end of a restricted arm of a very shallow ocean (Fig. 2A). Doubt that such a catastrophic pH or redox perturbation of the ocean was possible have come other indications that isotopic anomalies were meteoritic diagenesis (Kennedy 1996; Klaebe et al. 2017; Ahm et al. 2019). Some of the extremely negative isotopic anomalies in so-called "cap carbonates" were calcareous loess, comparable with the late Quaternary Peoria Loess of North America (Swineford and Frye 1951; Fisk 1951; Ruhe and Olson 1980; Grimley et al. 1998; Bettis et al. 2003). Multiple lines of evidence suggest such an origin for the Nuccaleena Formation above the basal Ediacaran stratotype locality in Enorama Creek, South Australia: thufur mounds, climbing translent stratification, tent structures with uniquely alternating top sets, and silt grain size (Retallack 2011a).

Another example of evidence for paleosols hiding in plain sight is the degree of sediment oxidation from highly reactive to total iron ratios (Fe_{HR}/Fe_T) in the Chuar Group (Johnston et al. 2010). Studies of modern coastal sediments show that Fe_{HR}/Fe_T ratio is >0.38 in anoxic shales with abundant pyrite, but less than that in well oxygenated shales (Canfield et al. 2007), but Fe_{HR}/Fe_T ratios <0.2 are only found in well drained soils (Ku et al. 2008). In the Chuar Group Fe_{HR}/Fe_T ratio is <0.2 is reliably found wherever there are red or purple paleosols and strongly negative $\delta^{13}C_{carb}$. and $\delta^{13}C_{org}$. values (Fig. 5G-H). A range of Fe_{HR}/Fe_T ratios are seen throughout the Chuar Group, with oscillations to values <0.2 over only a few meters, similar to Ediacaran redox fluctuations (Retallack 2016a). It now seems more likely that this reflects marine regression and soil formation rather than highly volatile marine redox. Such geochemical extremes are unusual for oceans, but are unremarkable within paleosols over only a few centimeters from the fully oxidized surface to the stagnant water table below (Retallack et al. 2014).

Our study of the Chuar group and review of comparable chemostratigraphic time series elsewhere (Dehler et al. 2017) reveal that the cause of isotopic variation is not oceanic chemical variation (Dehler et al. 2005; Corkeron 2007, 2008; Halverson et al. 2010; Swanson-Hysell et al. 2012), but episodic exposure and soil formation. This does not mean that chemostratigraphic correlation should be abandoned. Glacioeustatic sea level variation is a powerful tool for Phanerozoic

international correlation (Beu and Edwards 1984; Heckel et al. 1994), and from the Tonian to Ediacaran there were multiple glacial advances: Konnarock (752 Ma), Sturt (720 Ma), Elatina (635 Ma), Gaskiers (580 Ma), Fauquier (571 Ma), and Billy Springs (558 Ma) Glaciations (Hebert et al. 2010; Retallack et al. 2014, 2015; Pu et al. 2016). Sturt and Elatina Glaciations of the Cryogenian were the most extensive glaciations and also the most profound isotopic shifts (Corkeron 2007, 2008; Halverson et al. 2010; Swanson-Hysell et al. 2012), and the varying magnitude of glaciations is another tool for international correlation.

Declaration of Competing Interest

This is to certify that neither I, Gregory J. Retallack, nor my co-authors Adrian, P. Broz, Larry S.-H. Lai, and Kevin Gardner have any conflict of interest in publication of this article "*Neoproterozoic marine chemostratigraphy, or eustatic sea level change?*."

Acknowledgments

References

Abell, R., Thieme, M.L., Revenga, C., Bryer, M., Kottelat, M., Bogutskaya, N., Coad, B., Mandrak, N., Balderas, S.C., Bussing, W., Stiassny, M.L., 2008. Freshwater ecoregions of the world: a new map of biogeographic units for freshwater biodiversity conservation. BioScience 58, 403–414.

Agić, H., Högström, A.E., Moczydłowska, M., Jensen, S., Palacios, T., Meinhold, G., Ebbestad, J.O.R., Taylor, W.L., Høyberget, M., 2019. Organically-preserved multicellular eukaryote from the early Ediacaran Nyborg Formation, Arctic Norway. Sci. Rep. 9, 1–12.

Ahm, A.S.C., Maloof, A.C., Macdonald, F.A., Hoffman, P.F., Bjerrum, C.J., Bold, U., Rose, C.V., Strauss, J.V., Higgins, J.A., 2019. An early diagenetic deglacial origin for basal Ediacaran "cap dolostones". Earth Planet. Sci. Lett. 506, 292–307.

Aiello, I.W., Garrison, R.E., Moore, E.C., Kastner, M., Stakes, D.S., 2001. Anatomy and origin of carbonate structures in a Miocene cold-seep field. Geology 29, 1111–1114.

Al-Kofahi, M.M., Hallak, A.B., Al-Juwair, H.A., Saafin, A.K., 1993. Analysis of desert rose using PIXE and RBS techniques. X-Ray Spectrom. 22, 23–27.

Álvaro, J.J., Van Vliet-Lanoë, B., Vennin, E., Blanc-Valleron, M.M., 2003. Lower Cambrian paleosols from the Cantabrian Mountains (northern Spain): a comparison with Neogene–Quaternary estuarine analogues. Sediment. Geol. 163, 67–84.

Araya, J.P., González, M., Cardinale, M., Schnell, S., Stoll, A., 2020. Microbiome dynamics associated with the Atacama flowering desert. Front. Microbiol. 10, 3160.

Arnscheidt, C.W., Rothman, D.H., 2020. Routes to global glaciation. Proc. Roy. Soc. London A476, 20200303.

Bao, H., Chen, Z.Q., Zhou, C., 2012. An ^{17}O record of late Neoproterozoic glaciation in the Kimberley region, Western Australia. Precambrian Res. 216, 152–161.

Barbour, M.M., Farquhar, G.D., 2000. Relative humidity- and ABA-induced variation in carbon and oxygen isotope ratios of cotton leaves. Plant Cell Environ. 23, 473–485.

Barbour, M.M., Walcroft, A.S., Farquhar, G.D., 2002. Seasonal variation in d^{13}C and d^{18}O of cellulose from growth rings of *Pinus radiata*. Plant Cell Environ. 25, 1483–1499.

Barreda, V.D., Zamaloa, M.D.C., Gandolfo, M.A., Jaramillo, C., Wilf, P., 2020. Early Eocene Spore and Pollen Assemblages from the Laguna del Hunco Fossil Lake Beds, Patagonia. Argentina. Int. J. Plant Sci. 181, 594–615.

Belnap, J., Kaltenecker, J.H., Rosentreter, R., Williams, J., Leonard, S., Eldridge, D., 2001. Biological soil crusts: ecology and management. Bur. Land Manage. Techn. Ref. 1730, 1–110.

Berner, R.A., 1997. The rise of plants and their effect on weathering and atmospheric CO$_2$. Science 276, 543–546.

Bestland, E.A., Retallack, G.J., Rice, A.E., Mindszenty, A., 1996. Late Eocene detrital laterites in Central Oregon: mass balance geochemistry, depositional setting and landscape evolution. Bull. Geol. Soc. Am. 108, 285–302.

Bettis, E.A., Mason, J.P., Swinehart, J.B., Miao, X.-D., Hanson, P.R., Goble, R.J., Loope, D.B., Jacobs, P.M., Roberts, H.M., 2003. Cenozoic eolian sedimentary systems of the USA mid-continent. In: Easterbook, D.J. (Ed.), Quaternary geology of the

United States. INQUA 2003 field guide volume. Desert Research Institute, Reno, pp. 195–218.

Beu, A.G., Edwards, A.R., 1984. New Zealand Pleistocene and late Pliocene glacio-eustatic cycles. Palaeogeogr. Palaeoclim. Palaeoec. 46, 119–142.

Bloeser, B., 1985. *Melanocyrillium*, a new genus of structurally complex late Proterozoic microfossils from the Kwagunt Formation (Chuar Group), Grand Canyon. Arizona. J. Paleont. 59, 741–765.

Bonneville, S., Delpomdor, F., Préat, A., Chevalier, C., Araki, T., Kazemian, M., Steele, A., Schreiber, A., Wirth, R., Benning, L.G., 2020. Molecular identification of fungi microfossils in a Neoproterozoic shale rock. Science advances 6 eaax7599.

Brady, P.V., Dorn, R.I., Brazel, A.J., Clark, J., Moore, R.B., Glidewell, T., 1999. Direct measurement of the combined effects of lichen, rainfall, and temperature on silicate weathering. Geochim. Cosmochim. Acta 63, 3293–3300.

Breecker, D.O., Retallack, G.J., 2014. Refining the pedogenic carbonate atmospheric CO$_2$ proxy and application to Miocene CO$_2$. Palaeogeogr. Palaeoclim. Palaeoec. 406, 1–8.

Brimhall, G.H., Chadwick, O.A., Lewis, C.J., Compston, W., Williams, I.S., Danti, K.J., Dietrich, W.E., Power, M.E., Hendricks, D., Bratt, J., 1992. Deformational mass transport and invasive processes in soil evolution. Science 255, 695–702.

Brocks, J.J., Jarrett, A.J., Sirantoine, E., Hallmann, C., Hoshino, Y., Liyanage, T., 2017. The rise of algae in Cryogenian oceans and the emergence of animals. Nature 548, 578–581.

Bullard, A.R., 2018. New CA-ID-TIMS Detrital Zircon Constraints on Middle Neoproterozoic Sedimentary Successions, Southwestern United States. Utah State University, Logan, M.Sc. theis. https://digitalcommons.usu.edu/etd/7324.

Butler, R.F., 1992. Palaeomagnetism: Magnetic Domains to Geologic Terranes. Blackwell, Oxford, 336 p.

Canfield, D.E., Poulton, S.W., Narbonne, G.M., 2007. Late Neoproterozoic deep-ocean oxygenation and the rise of animal life. Science 315, 92–95.

Castillo, R.V., Beck, A., 2012. Photobiont selectivity and specificity in *Caloplaca* species in a fog-induced community in the Atacama Desert, northern Chile. Fungal Biology 116, 665–676.

Chadwick, O.A., Brimhall, G.H., Hendricks, D.M., 1990. From a black to a gray box—a mass balance interpretation of pedogenesis. Geomorphology 3, 369–390.

Chen, S., Gagnon, A.C., Adkins, J.F., 2018. Carbonic anhydrase, coral calcification, and a new model of stable isotope vital effects. Geochim. Cosmochim. Acta 236, 179–197.

Cockbain, A.E., 1976. Modern algal stromatolites at Hamelin Pool, a hypersaline barred basin in Shark Bay, Western Australia. In: Walter, M.R. (Ed.), Stromatolites. Elsevier, Amsterdam, pp. 389–411.

Coffey, J.M., Flannery, D.T., Walter, M.R., George, S.C., 2013. Sedimentology, stratigraphy and geochemistry of a stromatolite biofacies in the 2.72 Ga Tumbiana Formation, Fortescue Group, Western Australia. Precambrian Res. 236, 282–296.

Collins, L.B., Jahnert, R.J., 2014. Stromatolite research in the Shark Bay world heritage area. J. R. Soc. West. Australia 97, 189–219.

Cook, D.A., 1991. Sedimentology and Shale Petrology of the Upper Proterozoic Walcott Member Kwagunt Formation, Chuar Group, Grand Canyon, Arizona. Northern Arizona University, MSc thesis, 158 p.

Corkeron, M., 2007. 'Cap carbonates' and Neoproterozoic glacigenic successions from the Kimberley region, Northwest Australia. Sedimentology 54, 871–903.

Corkeron, M., 2008. Deposition and palaeogeography of a glacigenic Neoproterozoic succession in the East Kimberley, Australia. Sediment. Geol. 204, 61–82.

Corkeron, M., Webb, G.E., Moulds, J., Grey, K., 2012. Discriminating stromatolite formation modes using rare earth element geochemistry: Trapping and binding versus *in situ* precipitation of stromatolites from the Neoproterozoic Bitter Springs Formation, Northern Territory. Australia. Precambrian Res. 212, 194–206.

Crits-Christoph, A., Robinson, C.K., Barnum, T., Fricke, W.F., Davila, A.F., Jedynak, B., McKay, C.P., DiRuggiero, J., 2013. Colonization patterns of soil microbial communities in the Atacama Desert. Microbiome 1, 1–13.

Dalrymple, R.W., Narbonne, G.M., Smith, L., 1985. Eolian action and the distribution of Cambrian shales in North America. Geology 13, 607–610.

Dehler, C.M., Elrick, M., Karlstrom, K.E., Smith, G.A., Crossey, L.J., Timmons, J.M., 2001. Neoproterozoic Chuar Group (~ 800–742 Ma), Grand Canyon: a record of cyclic marine deposition during global cooling and supercontinent rifting. Sediment. Geol. 141, 465–499.

Dehler, C.M., Elrick, M., Bloch, J.D., Crossey, L.J., Karlstrom, K.E., Des Marais, D.J., 2005. High-resolution δ^{13}C stratigraphy of the Chuar Group (ca. 770–742 Ma), Grand Canyon: Implications for mid-Neoproterozoic climate change. Geol. Soc. Amer. Bull. 117, 32–45.

Dehler, C., Gehrels, G., Porter, S., Heizler, M., Karlstrom, K., Cox, G., Crossey, L., Timmons, M., 2017. Synthesis of the 780–740 Ma Chuar, Uinta Mountain, and Pahrump (ChUMP) groups, western USA: Implications for Laurentia-wide cratonic marine basins. Geol. Soc. Amer. Bull. 129, 607–624.

Dekov, V.M., Scholten, J., Botz, R., Garbe-Schönberg, C.-D., Thiry, M., Stoffers, P., Schmidt, M., 2005. Occurrence of kaolinite and mixed-layer kaolinite/smectite in hydrothermal sediments of Grimsey Graben, Tjörnes Fracture Zone (north of Iceland). Mar. Geol. 215, 159–170.

Donnadieu, Y., Goddéris, Y., Ramstein, G., Nédélec, A., Meert, J., 2004. A 'snowball Earth' climate triggered by continental break-up through changes in runoff. Nature 428, 302–306.

Driese, S.G., 2004. Pedogenic translocation of Fe in modern and ancient Vertisols and implications for interpretations of the Hekpoort paleosol (2.25 Ga). J. Geol. 112, 543–560.

Driese, S.G., Simpson, E.L., Eriksson, K.A., 1995. Redoximorphic Paleosols in alluvial and lacustrine deposits, 1.8 Ga Lochness Formation, Mount Isa, Australia; pedogenic processes and implications for paleoclimate. J. Sediment. Res. 65, 675–689.

Verrecchia, E.P., Dumont, J.-L., Verrecchia, K.E., 1993. Role of calcium cxalate biomineralization by fungi in the formation of calcretes: a case study from Nazareth. Israel. J. Sedim. Petrol. 63, 1000–1006.

Ehleringer, J.R., Cook, C.S., 1998. Carbon and oxygen isotope ratios of ecosystem respiration along an Oregon conifer transect: preliminary observations based on small flask sampling. Tree Physiol. 18, 513–519.

Ehleringer, J.R., Buchmann, N., Flanagan, L.B., 2000. Carbon isotope ratios in belowground carbon cycle processes. Ecol. Appl. 10, 412–422.

Elston, D.P., 1979. Late Precambrian Sixtymile Formation and orogeny at top of the Grand Canyon Supergroup, northern Arizona. U.S. Geol. Surv. Prof. Publ. 1092, 1–20.

Ewing, S.A., Sutter, B., Owen, J., Nishiizumi, K., Sharp, W., Cliff, S.S., Perry, K., Dietrich, W., McKay, C.P., Amundson, R., 2006. A threshold in soil formation at Earth's arid-hyperarid transition. Geochim. Cosmochim. Acta 70, 5291–5322.

Ewing, S.A., MacAlady, J.L., Warren-Rhodes, K., McKay, C.P., Amundson, R., 2008. Changes in the soil C cycle at the arid-hyperarid transition in the Atacama Desert. J. Geophys. Res. Biogeosciences 113 e G02S90.

Eyster, A., Weiss, B.P., Karlstrom, K., Macdonald, F.A., 2020. Paleomagnetism of the Chuar Group and evaluation of the late Tonian Laurentian apparent polar wander path with implications for the makeup and breakup of Rodinia. Geol. Soc. Amer. Bull. 132, 710–738.

Farquhar, G.D., Cernusak, L.A., 2012. Ternary effects on the gas exchange of isotopologues of carbon dioxide. Plant Cell Environ. 35, 1221–1231.

Fehrenbacher, J.B., Olson, K.R., Jansen, I.J., 1986. Loess thickness and its effect on soils in Illinois. Bulletin/University of Illinois at Urbana-Champaign. Illinois Agric. Exp. Stat. Bull. 782, 14 p.

Feulner, G., Hallmann, C., Kienert, H., 2015. Snowball cooling after algal rise. Nat. Geosci. 8, 659–662.

Filippelli, G.M., 2011. Phosphate rock formation and marine phosphorus geochemistry: the deep time perspective. Chemosphere 84, 759–766.

Fisk, H.N., 1951. Loess and Quaternary geology of the lower Mississippi Valley. J. Geol. 50, 333–356.

Food and Agriculture Organization, 1971. Soil Map of the World 1:5,000,000, vol. IV. South America, UNESCO, Paris, 193 p.

Food and Agriculture Organization, 1975a. Soil Map of the World 1:5,000,000, vol. II. North America, UNESCO, Paris, 210 p.

Food and Agriculture Organization, 1975b. Soil Map of the World 1:5,000,000, vol. III. Mexico and Central America, UNESCO, Paris, 96 p.

Food and Agriculture Organization, 1977. Soil Map of the World 1:5,000,000, vol. VII. South America, UNESCO, Paris, 117 p.

Ford, T.D., Breed, W.J., 1973. Late Precambrian Chuar Group, Grand Canyon. Arizona. Geol. Soc. Amer. Bull. 84, 1,243–1,260.

Ford, T.D., Breed, W.J., 1977. *Chuaria circularis* Walcott and other Precambrian fossils from the Grand Canyon. J. Palaeont. Soc. India 20, 170–177.

Gallagher, T.M., Sheldon, N.D., 2013. A new paleothermometer for forest paleosols and its implications for Cenozoic climate. Geology 41, 647–650.

Garcia-Pichel, F., Wojciechowski, M.F., 2009. The evolution of a capacity to build supra-cellular ropes enabled filamentous cyanobacteria to colonize highly erodible substrates. PLoS One 4, e7801.

Gehling, J.G., Droser, M.L., 2013. How well do fossil assemblages of the Ediacara biota tell time? Geology 41, 447–450.

Gernon, T.M., Hincks, T.K., Tyrrell, T., Rohling, E.J., Palmer, M.R., 2016. Snowball Earth Ocean chemistry driven by extensive ridge volcanism during Rodinia breakup. Nat. Geosci. 9, 242–248.

Giddings, J.A., Wallace, M.W., Haines, P.W., Mornane, K., 2010. Submarine origin for the Neoproterozoic Wonoka canyons, South Australia. Sediment. Geol. 223, 35–50.

Giordani, P., Modenesi, P., Tretiach, M., 2003. Determinant factors for the formation of the calcium oxalate minerals, weddellite and whewellite, on the surface of foliose lichens. Lichenologist 35, 255–270.

Grazhdankin, D., Gerdes, G., 2007. Ediacaran microbial colonies. Lethaia 40, 201–210.

Grazhdankin, D.V., Goy, Y.Y., Maslov, A.V., 2012. Late Riphean microbial colonies adapted to desiccating environments. Doklady Earth Sci. 446, 1157–1161.

Grimley, D.A., Follmer, L.R., McKay, E.D., 1998. Magnetic susceptibility and mineral zonation controlled by provenance in loess along the Illinois and Central Mississippi Valley. Quat. Res. 49, 24–36.

Grotzinger, J.P., Fike, D.A., Fischer, W.W., 2011. Enigmatic origin of the largest-known carbon isotope excursion in Earth's history. Nat. Geosci. 4, 285–292.

Haile, N.S., 1975. Calculation of paleolatitudes from paleomagnetic poles. Geology 3, 174.

Halverson, G.P., Wade, B.P., Hurtgen, M.T., Barovich, K.M., 2010. Neoproterozoic chemostratigraphy. Precambrian Res. 182, 337–350.

Harden, J.W., 1982. A quantitative index of soil development from field descriptions: examples from a chronosequence in Central California. Geoderma 28, 1–28.

Harsch, M.A., Bader, M.Y., 2011. Treeline form–a potential key to understanding treeline dynamics. Glob. Ecol. Biogeogr. 20, 582–596.

Hay, C.C., Creveling, J.R., Hagen, C.J., Maloof, A.C., Huybers, P., 2019. A library of early Cambrian chemostratigraphic correlations from a reproducible algorithm. Geology 47, 457–460.

Hayes, J.L., Riebe, C.S., Holbrook, S.W., Flinchum, B.A., Hartsough, P.C., 2019. Porosity production in weathered rock: where volumetric strain dominates over chemical mass loss. Sci. Adv. 5, 1–12.

Hebert, C.L., Kaufman, A.J., Penniston-Dorland, S.C., Martin, A.J., 2010. Radiometric and stratigraphic constraints on terminal Edicaran (post-Gaskiers) glaciation and metazoan evolution. Precambrian Res. 182, 402–414.

Heckel, P.H., Dennison, J.M., Ettensohn, F.R., 1994. Evaluation of evidence for glacio-eustatic control over marine Pennsylvanian cyclothems in North America and consideration of possible tectonic effects. In: Dennison, J.M.; Ettensohn, F.R. (Eds), Tectonic and eustatic controls on sedimentary cycles. Soc. Econ. Palent. Mineral., Tulsa, Concepts Sediment. Paleont 4, 65–87.

Hedges, S.B., 2003. Molecular clocks and a biological trigger for Neoproterozoic Snowball Earth events and the Cambrian explosion. In: Donoghue, P.C.J., Smith, P. M. (Eds.), Telling the Evolutionary Time: Molecular Clocks and the Fossil Record. CRC press, Boca Raton, pp. 27–40.

Hoffman, P.F., Li, Z.X., 2009. A palaeogeographic context for Neoproterozoic glaciation. Palaeogeogr. Palaeoclim. Palaeoec. 277, 158–172.

Hoffman, P.F., Schrag, D.P., 2002. The Snowball Earth hypothesis: testing the limits of global change. Terra Nova 14, 139–155.

Hoffman, P.F., Kaufman, A.J., Halverson, G.P., Schrag, D.P., 1998. A Neoproterozoic snowball earth. Science 281, 1342–1346.

Hofmann, H.J., 1977. The problematic fossil *Chuaria* from the late Precambrian Uinta mountain group. Utah. Precambrian Res. 4, 1–11.

Hofmann, H.J., Narbonne, G.M., Aitken, J.D., 1990. Ediacaran remains from the intertillite beds, northwestern Canada. Geology 18, 1199–1202.

Horodyski, R.J., 1993. Paleontology of Proterozoic shales and mudstones: examples from the Belt supergroup, Chuar Group and Pahrump Group, western USA. Precambrian Res. 61, 241–278.

Horodyski, R.J., Bloeser, B., 1983. Possible eukaryotic algal filaments from the late Proterozoic Chuar Group, Grand Canyon. Arizona. J. Paleont. 57, 321–326.

Huang, C.-M., Wang, C.-S., Tang, Y., 2005. Stable carbon and oxygen isotopes of pedogenic carbonates in Ustic Vertisols: implications for paleoenvironmental change. Pedosphere 15, 539–544.

Husson, J.M., Maloof, A.C., Schoene, B., 2012. A syn-depositional age for Earth's deepest $\delta^{13}C$ excursion required by isotope conglomerate tests. Terra Nova 24, 318–325.

Isbell, R.F., 1996. The Australian Soil Classification, revised edition. CSIRO Publishing, Collingwood. 144 pp.

Jago, J.B., Gehling, J.G., Paterson, J.R., Brock, G.A., 2012. Comments on Retallack, G.J. 2011: problematic megafossils in Cambrian palaeosols of South Australia. Palaeontology 55, 913–917.

Johnson, N.G., 1985. Early Silurian palynomorphs from the Tuscarora Formation in Central Pennsylvania and their paleobotanical and geological significance. Rev. Palaeobot. Palynol. 45, 307–359.

Johnston, D.T., Poulton, S.W., Dehler, C., Porter, S., Husson, J., Canfield, D.E., Knoll, A. H., 2010. An emerging picture of Neoproterozoic Ocean chemistry: Insights from the Chuar Group, Grand Canyon. USA. Earth Planet. Sci. Lett. 290, 64–73.

Karlstrom, K.E., Bowring, S.A., Dehler, C.M., Knoll, A.H., Porter, S.M., Marais, D.J.D., Weil, A.B., Sharp, Z.D., Geissman, J.W., Elrick, M.B., Timmons, J.M., 2000. Chuar Group of the Grand Canyon: Record of breakup of Rodinia, associated change in the global carbon cycle, and ecosystem expansion by 740 Ma. Geology 28, 619–622.

Karlstrom, K., Hagadorn, J., Gehrels, G., Matthews, W., Schmitz, M., Madronich, L., Mulder, J., Pecha, M., Giesler, D., Crossey, L., 2018. Cambrian Sauk transgression in the Grand Canyon region redefined by detrital zircons. Nat. Geosci. 11, 438–443.

Karlstrom, K.E., Mohr, M.T., Schmitz, M.D., Sundberg, F.A., Rowland, S.M., Blakey, R., Foster, J.R., Crossey, L.J., Dehler, C.M., Hagadorn, J.W., 2020. Redefining the Tonto Group of Grand Canyon and recalibrating the Cambrian time scale. Geology 48, 425–430.

Kelka, U., Veveakis, M., Koehn, D., Beaudoin, N., 2017. Zebra rocks: compaction waves create ore deposits. Sci. Rep. 7 (1), 1–9.

Kennedy, M.J., 1996. Stratigraphy, sedimentology, and isotopic geochemistry of Australian Neoproterozoic postglacial cap dolostones; deglaciation, $\delta^{13}C$ excursions, and carbonate precipitation. J. Sediment. Res. 66, 1050–1064.

Kennedy, M.J., 2013. The nonlinear effects of evolutionary innovation biospheric feedbacks on qualitative environmental change: from the microbial to metazoan world. Amer. Naturalist 81, 100–111.

Kennedy, M., Droser, M., Mayer, L.M., Pevear, D., Mrofka, D., 2006. Late Precambrian oxygenation; inception of the clay mineral factory. Science 311, 1446–1449.

Kennedy, M., Mrofka, D., Von Der Borch, C., 2008. Snowball Earth termination by destabilization of equatorial permafrost methane clathrate. Nature 453, 642–645.

Kirschvink, J., 1992. Late Proterozoic low-latitude global glaciation: The Snowball Earth. In: Schopf, J.W., Klein, C. (Eds.), The Proterozoic Biosphere. Cambridge University Press, New York, pp. 51–52.

Klaebe, R.M., Kennedy, M.J., Jarrett, A.J.M., Brocks, J.J., 2017. Local paleoenvironmental controls on the carbon-isotope record defining the Bitter Springs Anomaly. Geobiology 15, 65–80.

Knauth, L.P., Kennedy, M.J., 2009. The late Precambrian greening of the Earth. Nature 460, 728–732.

Knauth, L.P., Brilli, M., Klonowski, S., 2003. Isotope geochemistry of caliche developed on basalt. Geochim. Cosmochim. Acta 67, 185–195.

Knoll, A.H., Golubic, S., 1992. Proterozoic and living cyanobacteria. In: Schidlowski, M., Golubic, S., Kimberley, M.M., McKirdy, D.M., Trudinger, P.A. (Eds.), Early Organic Evolution: Implications for Mineral and Energy Resources. Springer, Berlin, pp. 450–462.

Kokelj, S.V., Pisaric, M.F.J., Burns, C.R., 2007. Cessation of ice-wedge development during the 20th century in spruce forests of eastern Mackenzie Delta, Northwest Territories, Canada. Canad. J. Earth Sci. 44, 1503–-1515.

Komar, P.D., 1985. The hydraulic interpretation of turbidites from their grain sizes and sedimentary structures. Sedimentology 32, 395–407.

Korsch, R.J., Roser, B.P., Kamprad, J.L., 1993. Geochemical, petrographic and grain-size variations within single turbidite beds. Sediment. Geol. 83, 15–35.

Ku, T.C.W., Kay, J., Browne, E., Martini, A.M., Peters, S.C., Chen, M.D., 2008. Pyritization of iron in tropical coastal sediments: implications for the development of iron, sulfur, and carbon diagenetic properties, Saint Lucia. Lesser Antilles. Marine Geol. 249, 184–205.

Kumar, S., 2001. Mesoproterozoic megafossil *Chuaria–Tawuia* association may represent parts of a multicellular plant, Vindhyan Supergroup, Central India. Precambrian Res 106, 187–211.

Lenton, T.M., Crouch, M., Johnson, M., Pires, N., Dolan, L., 2012. First plants cooled the Ordovician. Nat. Geosci. 5, 86–89.

Li, Z.X., Evans, D.A.D., Halverson, G.P., 2013. Neoproterozoic glaciations in a revised global palaeogeography from the breakup of Rodinia to the assembly of Gondwanaland. Sedimentary Geol. 294, 219–232.

Liivamägi, S., Somelar, P., Mahaney, W.C., Kirs, J., Vircava, I., Kirsimäe, K., 2014. Late Neoproterozoic Baltic paleosol: intense weathering at high latitude? Geology 42, 323–326.

Lohmann, K.G., 1988. Geochemical patterns of meteoric diagenetic systems and their application to studies of paleokarst. In: James, N.P., Choquette, P.W. (Eds.), Paleokarst. Springer, Berlin, pp. 59–80.

Long, J., Zhang, S., Luo, K., 2019. Cryogenian magmatic activity and early life evolution. Sci. Rep. 9, 6586.

Loron, C.C., François, C., Rainbird, R.H., Turner, E.C., Borensztajn, S., Javaux, E.J., 2019. Early fungi from the Proterozoic era in Arctic Canada. Nature 570, 232–235.

Ludvigson, G.A., González, L.A., Metzger, R.A., Witzke, B.J., Brenner, R.L., Murillo, A.P., White, T.S., 1998. Meteoric sphaerosiderite lines and their use for paleohydrology and paleoclimatology. Geology 26, 1039–1042.

Ludvigson, G.A., González, L.A., Fowle, D.A., Roberts, J.A., Driese, S.G., Villarreal, M.A., Smith, J.J., Suarez, M.B., Nordt, L.C., 2013. Paleoclimatic applications and modern process studies of pedogenic siderite. In: Driese, S.G., Nordt, L.C. (Eds.), New Frontiers in Paleopedology and Terrestrial Paleoclimatology, Soc. Econ. Paleont. Mineral. Spec. Publ, vol. 104, pp. 79–87.

Macdonald, F.A., Wordsworth, R., 2017. Initiation of Snowball Earth with volcanic sulfur aerosol emissions. Geophys. Res. Lett. 44, 1938–1946.

MacLennan, S.A., Eddy, M.P., Merschat, A.J., Mehra, A.K., Crockford, P.W., Maloof, A.C., Southworth, C.S., Schoene, B., 2020. Geologic evidence for an icehouse Earth before the Sturtian global glaciation. Sci. Adv. 6 (24), 6647.

van Maldegem, L.M., Sansjofre, P., Weijers, J.W., Wolkenstein, K., Strother, P.K., Wörmer, L., Hefter, J., Nettersheim, B.J., Hoshino, Y., Schouten, S., Damsté, J.S.S., 2019. Bisnorgammacerane traces predatory pressure and the persistent rise of algal ecosystems after Snowball Earth. Nat. Commun. 10 (1), 1–11.

Marumo, K., Hattori, K.H., 1999. Seafloor hydrothermal clay alteration at Jade in the back-arc Okinawa Trough: Mineralogy, geochemistry and isotope characteristics. Geochim. Cosmochim. Acta 63, 2785–2804.

Melim, L.A., Swart, P.K., Eberli, G.P., 2004. Mixing zone diagenesis in the subsurface of Florida and the Bahamas. J. Sedim. Res. 76, 904–913.

Méndez, W., Cartaya, S., 2001. Ambientes depositacionales recientes y evolución geomorfológica del complejo sedimentario isla barrera–laguna litoral de la salina de Sauca, Falcón nororiental. Venezuela. Bol. Soc. Venezol. Geól. 26, 8–35.

Merkel, A., 2020. Climate Data for Cities Worldwide. Website. https://en.climate-data.org.

Morteani, G., Ackermand, D., Trappe, J., 2007. Aluminum phosphate in Proterozoic metaquartzites: Implications for the Precambrian oceanic P. budget and development of life. In: Linneman, U., Nance, R.D., Kraft, P., Zulauf, G. (Eds.), The Evolution of the Rheic Ocean: From Avalonian-Cadomian Active Margin to Alleghenian-Variscan Collision, Geol. Soc. Amer. Spec. Pap, vol. 423, pp. 579–592.

Murphy, C.P., 1983. Point counting pores and illuvial clay in thin section. Geoderma 31, 133–150.

Navarro-González, R., Rainey, F.A., Molina, P., Bagaley, D.R., Hollen, B.J., de la Rosa, J., Small, A.M., Quinn, R.C., Grunthaner, F.J., Cáceres, L., Gomez-Silva, B., 2003. Mars-like soils in the Atacama Desert, Chile, and the dry limit of microbial life. Science 302, 1018–1021.

Neaman, A., Chorover, J., Brantley, S.L., 2005a. Element mobility patterns record organic ligands in soils on early Earth. Geology 33, 117–120.

Neaman, A., Chorover, J., Brantley, S.L., 2005b. Implications of the evolution of organic acid moieties for basalt weathering over geological time. Amer. J. Sci. 305, 147–185.

Neilson, J.W., Quade, J., Ortiz, M., Nelson, W.M., Legatzki, A., Tian, F., LaComb, M., Betancourt, J.L., Wing, R.A., Soderlund, C.A., Maier, R.M., 2012. Life at the hyperarid margin: novel bacterial diversity in arid soils of the Atacama Desert, Chile. Extremophiles 16, 553–566.

Neilson, J.W., Califf, K., Cardona, C., Copeland, A., Van Treuren, W., Josephson, K.L., Knight, R., Gilbert, J.A., Quade, J., Caporaso, J.G., Maier, R.M., 2017. Significant impacts of increasing aridity on the arid soil microbiome. MSystems 2, e00195–16.

Nesbitt, H.W., Young, G.M., 1982. Early Proterozoic climates and plate motions inferred from major element chemistry of lutites. Nature 299, 715–717.

Novoselov, A.A., de Souza Filho, C.R., 2015. Potassium metasomatism of Precambrian paleosols. Precambrian Res. 262, 67–83.

Ohnemueller, F., Prave, A.R., Fallick, A.E., Kasemann, S.A., 2014. Ocean acidification in the aftermath of the Marinoan glaciation. Geology 42, 1103–1106.

Óskarsson, B.V., Riishuus, M.S., Arnalds, Ó., 2012. Climate-dependent chemical weathering of volcanic soils in Iceland. Geoderma 189, 635–651.

Papazzoni, C.A., Carnevale, G., Fornaciari, E., Giusberti, L., Trevisani, E., 2014. The Pesciara-Monte Postale Fossil-Lagerstätte: 1. Biostratigraphy, sedimentology and depositional model. The Bolca Fossil-Lagerstätte: a Window into the Eocene World. Rendic. Soc. Paleont. Italiana 4, 29–36.

Peckmann, J., Goedert, J.L., Thiel, V., Michaelis, W., Reitner, J., 2002. A comprehensive approach to the study of methane-seep deposits from the Lincoln Creek Formation, western Washington State, USA. Sedimentology 49, 855–873.

Plummer, P.S., Gostin, V.A., 1981. Shrinkage cracks; desiccation or synaeresis? J. Sediment. Res. 51, 1147–1156.

Porter, S.M., 2016. Tiny vampires in ancient seas: evidence for predation via perforation in fossils from the 780–740 million-year-old Chuar Group, Grand Canyon, USA. Proc. R. Soc. B283, e.20160221.

Porter, S.M., Knoll, A.H., 2000. Testate amoebae in the Neoproterozoic Era: evidence from vase-shaped microfossils in the Chuar Group, Grand Canyon. Paleobiology 26, 360–385.

Porter, S.M., Riedman, L.A., 2016. Systematics of organic-walled microfossils from the ca. 780–740 Ma Chuar Group, Grand Canyon. Arizona. J. Paleont. 90, 815–853.

Porter, S.M., Meisterfeld, R., Knoll, A.H., 2003. Vase-shaped microfossils from the Neoproterozoic Chuar Group, Grand Canyon: a classification guided by modern testate amoebae. J. Paleontol. 77, 409–429.

Prave, A.R., 2002. Life on land in the Proterozoic: evidence from the Torridonian rocks of Northwest Scotland. Geology 30, 811–814.

Pu, J.P., Bowring, S.A., Ramezani, J., Myrow, P., Raub, T.D., Landing, E., Mills, A., Hodgin, E., Macdonald, F.A., 2016. Dodging snowballs: Geochronology of the Gaskiers glaciation and the first appearance of the Ediacaran biota. Geology 44, 955–958.

Pye, K., Sherwin, D., 1999. Loess. In: Goudie, A.S., Livingstone, I., Stokes, S. (Eds.), Aeolian Environments. Sediments and Landforms. Wiley, Chichester, pp. 213–238.

Quade, J., Rech, J.A., Latorre, C., Betancourt, J.L., Gleeson, E., Kalin, M.T., 2007. Soils at the hyperarid margin: the isotopic composition of soil carbonate from the Atacama Desert. Northern Chile. Geochim. Cosmochim. Acta 71, 3772–3795.

Raffi, R., Stenni, B., 2011. Isotopic composition and thermal regime of ice wedges in Northern Victoria Land, East Antarctica. Permafrost Periglacial Processes 22, 65- 83.

Rech, J.A., Quade, J., Hart, W.S., 2003. Isotopic evidence for the source of ca and S in soil gypsum, anhydrite and calcite in the Atacama Desert. Chile. Geochim. Cosmochim. Acta 67, 575–586.

Renaut, R.W., Tiecerlin, J.-J., 1994. Lake Bogoria, Kenya Rift Valley − a sedimentological overview. In: Renaut, R.W., Last, W.M. (Eds.), Sedimentology and Geochemistry of Modern and Ancient Saline Lakes, Soc. Sediment. Geol. Spec. Publ, vol. 50, pp. 101–124.

Retallack, G.J., 2008. Cambrian palaeosols and landscapes of South Australia. Austral. J. Earth Sci. 55, 1083–1106.

Retallack, G.J., 2011a. Neoproterozoic loess and limits to snowball Earth. J. Geol. Soc. 168 (2), 289–308.

Retallack, G.J., 2011b. Problematic megafossils in Cambrian palaeosols of South Australia. Palaeontology 54, 1223–1242.

Retallack, G.J., 2012a. Criteria for distinguishing microbial mats and earths. In: Noffke, N., Chafetz, H. (Eds.), Microbial Mats in Siliciclastic Sediments, Soc. Econ. Paleont. Mineral. Spec. Pap, vol. 101, pp. 136–152.

Retallack, G.J., 2012b. Reply to comments on Retallack 2011: problematic megafossils in Cambrian palaeosols of South Australia. Palaeontology 55, 919–921.

Retallack, G.J., 2013. Early Cambrian humid, tropical paleosols from Montana. In Driese, S.G. and Nordt, L., eds., New frontiers in paleopedology and terrestrial paleoclimatology. Soc. Econ. Paleont. Mineral., Tulsa. Spec. Pap. 44, 257–272.

Retallack, G.J., 2015a. Silurian vegetation stature and density inferred from fossil soils and plants in Pennsylvania, U.S.a. J. Geol. Soc. London 172, 693–709.

Retallack, G.J., 2015b. Late Ordovician glaciation initiated by early land plant evolution, and punctuated by greenhouse mass-extinctions. J. Geol. 123, 509–538.

Retallack, G.J., 2015c. Acritarch evidence for an Ediacaran adaptive radiation of Fungi. Botanica Pacifica 4, 19–33.

Retallack, G.J., 2016a. Ediacaran sedimentology and paleoecology of Newfoundland reconsidered. Sediment. Geol. 333, 15–31.

Retallack, G.J., 2016b. Field and laboratory tests for recognition of Ediacaran paleosols. Gondwana Res. 36, 94–110.

Retallack, G.J., 2019. Soils of the Past. Wiley, Chichester, 534 p.

Retallack, G., 2020. Boron paleosalinity proxy for deeply buried Paleozoic and Ediacaran fossils. Palaeogeogr. Palaeoclim. Palaeoec. 540, 109536.

Retallack, G.J., Marconato, A., Osterhout, J.T., Watts, K.E., Bindeman, I.N., 2014. Revised Wonoka isotopic anomaly in South Australia and late Ediacaran mass extinction. J. Geol. Soc. Lond. 171, 709–722.

Retallack, G.J., Gose, B.N., Osterhout, J.T., 2015. Periglacial paleosols and Cryogenian paleoclimate near Adelaide. South Australia. Precambrian Res. 263, 1–18.

Reynolds, M.W., Elston, D.P., 1986. Stratigraphy and sedimentation of part of the Proterozoic Chuar Group, Grand Canyon. Arizona. Geol. Soc. Amer. Abstr. Progr. 18 (5), 405.

Reynolds, M.W., Palacas, J.G., Elston, D.P., 1988. Potential petroleum source rocks in the late Proterozoic Chuar Group (Precambrian) in Grand Canyon, Arizona Cabs. In: Carter, L.M.H. (Ed.), V.E. McKelvey Forum on Mineral and Energy Resources: U.S. Geol. Surv. Circ. 1025, 49–50.

Rooney, A.D., Austermann, J., Smith, E.F., Li, Y., Selby, D., Dehler, C.M., Schmitz, M.D., Karlstrom, K.E., Macdonald, F.A., 2018. Coupled Re-Os and U-Pb geochronology of the Tonian Chuar Group, Grand Canyon. Geol. Soc. Amer. Bull. 130, 1085–1098.

Rosentreter, R., 1984. Compositional patterns within a rabbitbrush (*Chrysothamnus*) community of the Idaho Snake River Plain. Intermountain Res. Stat. Gen. Techn. Rept INT-200, 273–277.

Ruhe, R.V., Olson, C.G., 1980. Clay mineral indicators of glacial and non-glacial sources of Wisconsinan loesses in southern Indiana, USA. Geoderma 24, 283–297.

Schidlowski, M., 2001. Carbon isotopes as biogeochemical recorders of life over 3.8 Ga of Earth history: evolution of a concept. Precambrian Res. 106, 117–134.

Schopf, J.W., Ford, T.D., Breed, W.J., 1973. Microorganisms from the late Precambrian of the Grand Canyon, Arizona. Science 179, 1319–1321.

Sheldon, N.D., Retallack, G.J., 2001. Equation for compaction of paleosols due to burial. Geology 29, 247–250.

Sheldon, N.D., Tabor, N.J., 2013. Using paleosols to understand paleo-carbon burial. In: Dreise, S.G., Nordt, L. (Eds.), New Frontiers in Paleopedology and Terrestrial

Paleoclimatology: Paleosols and Soil Surface Analog Systems, Soc. Econ. Paleont. Mineral Spec. Publ, vol. 104, pp. 71–78.

Sheldon, N.D., Retallack, G.J., Tanaka, S., 2002. Geochemical climofunctions from north American soils and application to paleosols across the Eocene-Oligocene boundary in Oregon. J. Geol. 110, 687–696.

Sinyella, L., Crawford, J.M., 1984. Havasupai word list. Web page. https://berkeley.app. box.com/s/87jdy84m6noi29uo331v7grcgfmevjff/file.18339047376, 2 accessed September 25, 2019.

Smith, M.R., 2016. Cord-forming Palaeozoic fungi in terrestrial assemblages. Bot. J. Linnean Soc. 180, 452–460.

Soil Survey Staff, 2014. Keys to Soil Taxonomy. Natural Resources Conservation Service, Washington DC, 358 pp.

Southgate, P.N., 1986. Depositional environment and mechanism of preservation of microfossils, upper Proterozoic Bitter Springs Formation, Australia. Geology 14, 683–686.

Southgate, P.N., 1989. Relationships between cyclicity and stromatolite form in the late Proterozoic Bitter Springs Formation, Australia. Sedimentology 36, 323–339.

Stace, H.C.T., Hubble, G.D., Brewer, R., Northcote, K.H., Sleeman, J.R., Mulcahy, M.J., Hallsworth, E.G., 1968. A Handbook of Australian Soils. Rellim, Adelaide, 435 pp.

Stern, R.J., Miller, N.R., 2018. Did the transition to plate tectonics cause Neoproterozoic Snowball Earth? Terra Nova 30, 87–94.

Strother, P.K., Battison, L., Brasier, M.D., Wellman, C.H., 2011. Earth's earliest non-marine eukaryotes. Nature 473, 505–509.

Strother, P.K., Taylor, W.A., Beck, J.H., Vecoli, M., 2017. Ordovician spore 'thalli' and the evolution of the plant sporophyte. Palynology 41 (supp1), 57–68.

Surge, D.M., Savarese, M., Dodd, J.R., Lohmann, K.C., 1997. Carbon isotopic evidence for photosynthesis in early Cambrian oceans. Geology 25, 503–506.

Swanson-Hysell, N.L., Maloof, A.C., Kirschvink, J.L., Evans, D.A., Halverson, G.P., Hurtgen, M.T., 2012. Constraints on Neoproterozoic paleogeography and Paleozoic orogenesis from paleomagnetic records of the Bitter Springs Formation, Amadeus Basin, Central Australia. Amer. J. Sci. 312, 817–884.

Swineford, A., Frye, J.C., 1951. Petrography of the Peoria loess in Kansas. J. Geol. 59, 306–322.

Talbot, M.R., 1990. A review of the palaeohydrological interpretation of carbon and oxygen isotopic ratios in primary lacustrine carbonates. Chem. Geol. Isotope Geosci. Sect. 80, 261–279.

Terry, R.D., Chilingar, G.V., 1955. Summary of "concerning some additional aids in studying sedimentary formations," by MS Shvetsov. J. Sedim. Res. 25, 229–234.

Tziperman, E., Halevy, I., Johnston, D.T., Knoll, A.H., Schrag, D.P., 2011. Biologically induced initiation of Neoproterozoic snowball-Earth events. U.S. Nat. Acad. Sci. 108, 15091–15096.

Ufnar, D.F., Gröcke, D.R, Beddows, P.A., 2008. Assessing pedogenic calcite stable isotope values; can positive linear covariant trends be used to quantify palaeo-evaporation rates? Chem. Geol. 256, 46–51.

Van Maldegem, L.M., 2017. Molecular and isotopic signatures of life surrounding the Neoproterozoic Snowball Earth events. In: Doctoral Thesis, Univ. Bremen, 231 p.

Veizer, J., Ala, D., Azmy, K., Bruckschen, P., Buhl, D., Bruhn, F., Carden, G.A.F., Diener, A., Ebneth, S., Godderis, Y., Jasper, T., Korte, C., Pawellek, F., Podlaha, O.G., Strauss, H., 1999. ^{87}Sr/^{86}Sr, δ^{13}C and δ^{18}O evolution of Phanerozoic seawater. Chem. Geol. 161, 59–88.

Vepraskas, M.J., Sprecher, S.W., 1997. Overview of aquic conditions and hydric soils. In: Vepraskas, M.J., Sprecher, S.W. (Eds.), Aquic conditions and hydric soils: the problem soils. Soil Sci. Soc. Amer Spec. Publ.5 0, pp. 1–22.

Verdel, C., Niemi, N., van Der Pluijm, B.A., 2011. Variations in the illite to muscovite transition related to metamorphic conditions and detrital muscovite content: insight from the Paleozoic passive margin of the southwestern United States. J. Geol. 119, 419–437.

Vidal, G., Ford, T.D., 1985. Microbiotas from the late Proterozoic Chuar Group (northern Arizona) and Uinta Mountain Group (Utah) and their chronostratigraphic implications. Precambrian Res. 28, 349–389.

Vidal, G., Knoll, A.H., 1983. Proterozoic plankton. In: Medaris, L.G., Byers, C.W., Mickelson, C.M., Shanks, W.C. (Eds.), Proterozoic Geology: selected papers from an International Proterozoic Symposium. Geol. Soc. Amer. Mem, 161, pp. 265–277.

Vinogradov, A.P., 1959. Geochemistry of Rare and Dispersed Chemical Elements in Soils. Translated by Consultants Bureau, New York, 209 pp.

Vítek, P., Cámara-Gallego, B., Edwards, H.G., Jehlička, J., Ascaso, C., Wierzchos, J., 2013. Phototrophic community in gypsum crust from the Atacama Desert studied by Raman spectroscopy and microscopic imaging. Geomicrobiol J. 30, 399–410.

Wacey, D., Urosevic, L., Saunders, M., George, A.D., 2018. Mineralisation of filamentous cyanobacteria in Lake Thetis stromatolites, Western Australia. Geobiology 16, 203–215.

Wallace, M.W., Hood, A.S., 2018. Zebra textures in carbonate rocks: Fractures produced by the force of crystallization during mineral replacement. Sediment. Geol. 368, 58–67.

Walter, M.R., 1972. Stromatolites and the biostratigraphy of the Australian Precambrian and Cambrian. Spec. Pap. Palaeontology 11, 1–190.

Walter, M.R., 1976. Stromatolites. Elsevier, Amsterdam, 790 pp.

Watson, A., 1985. Structure, chemistry and origins of gypsum crusts in southern Tunisia and the central Namib Desert. Sedimentology 32, 855–875.

Weete, J.D., Abril, M., Blackwell, M., 2010. Phylogenetic distribution of fungal sterols. PLoS One 5 (5), e10899.

Weil, A.B., Geissman, J.W., Van Der Voo, R., 2004. Paleomagnetism of the Neoproterozoic Chuar Group, Grand Canyon Supergroup Arizona: Implications for Laurentia's Neoproterozoic APWP and Rodinia break-up. Precambrian Res. 129, 71–92.

Weinberger, R., 2001. Evolution of polygonal patterns in stratified mud during desiccation: the role of flaw distribution and layer boundaries. Geol. Soc. Amer. Bull 113, 20–31.

Wiley, B.H., Dehler, C.M., Ghazi, S.A., Kuo, L., Rauzi, S.L., 2001. Geologic description, sampling, and petroleum source rock potential of the Awatubi and Walcott Members, Kwagunt Formation Chuar Group of the Sixtymile Canyon Section, Grand Canyon, Arizona. Arizona Geol. Surv. Open File Rept. OFR-02-01 (84 p).

Yuan, X., Xiao, S., Taylor, T.N., 2005. Lichen-like symbiosis 600 million years ago. Science 308, 1017–1020.

Zakrzewska, B., 1963. An analysis of landforms in a part of the central Great Plains. Ann. Assoc. Amer. Geograph. 53, 536–568.

Ziegenbalg, S.B., Brunner, B., Rouchy, J.M., Birgel, D., Pierre, C., Böttcher, M.E., Caruso, A., Immenhauser, A., Peckmann, J., 2010. Formation of secondary carbonates and native Sulphur in sulphate-rich Messinian strata. Sicily. Sediment. Geol. 227, 37–50.

Zillen, L.M., Snowball, I.F., Sandgren, P., Stanton, T., 2003. Occurrence of varved lake sediment sequences in Vamtland, west Central Sweden: lake characteristics, varve chronology and AMS radiocarbon dating. Boreas 32, 612–626.

Zumberge, J.A., Rocher, D., Love, G.D., 2020. Free and kerogen-bound biomarkers from late Tonian sedimentary rocks record abundant eukaryotes in mid-Neoproterozoic marine communities. Geobiology 18, 326–347.